


Biomimetic and osteogenic 3D silk fibroin composite scaffolds with nano MgO and mineralized hydroxyapatite for bone regeneration

Ziquan Wu¹ , Zhulong Meng², Qianjin Wu¹, Delu Zeng¹, Zhengdong Guo¹, Jiangling Yao¹, Yangyang Bian¹, Yuntao Gu³, Shaowen Cheng¹, Lei Peng^{1,4} and Yingzheng Zhao⁵

Abstract

Artificial bioactive materials have received increasing attention worldwide in clinical orthopedics to repair bone defects that are caused by trauma, infections or tumors, especially dedicated to the multifunctional composite effect of materials. In this study, a weakly alkaline, biomimetic and osteogenic, three-dimensional composite scaffold (3DS) with hydroxyapatite (HAp) and nano magnesium oxide (MgO) embedded in fiber (F) of silkworm cocoon and silk fibroin (SF) is evaluated comprehensively for its bone repair potential in vivo and in vitro experiments, particularly focusing on the combined effect between HAp and MgO. Magnesium ions (Mg²⁺) has long been proven to promote bone tissue regeneration, and HAp is provided with osteoconductive properties. Interestingly, the weak alkaline microenvironment from MgO may also be crucial to promote Sprague-Dawley (SD) rat bone mesenchymal stem cells (BMSCs) proliferation, osteogenic differentiation and alkaline phosphatase (ALP) activities. This SF/F/HAp/nano MgO (SFFHM) 3DS with superior biocompatibility and biodegradability has better mechanical properties, BMSCs proliferation ability, osteogenic activity and differentiation potential compared with the scaffolds adding HAp or MgO alone or neither. Similarly, corresponding meaningful results are also demonstrated in a model of distal lateral femoral defect in SD rat. Therefore, we provide a promising 3D composite scaffold for promoting bone regeneration applications in bone tissue engineering.

Keywords

Silk fibroin, nano magnesium oxide, hydroxyapatite, composite scaffold, bone tissue engineering

Date received: 13 June 2020; accepted: 1 October 2020

Introduction

Bone defects caused by various diseases are common problems in clinical orthopaedics. To solve the problem, a variety of bone substitutes have been developed,¹ in particular, the application of bioactive 3DS for bone regeneration has received increasing attention. Among these materials, hydrogels inlaid with different bioactive metal and metal oxide nanoparticles, such as the compounds of Mg, Zn, Fe, Ti, Si and Sr element,^{2–5} have become research hotspots as they eventually can be absorbed or decomposed by newly formed bone tissue without foreign body rejection and secondary surgery.^{6,7} These biomaterials can be filled via minimally invasive injections to the bone irregular defect site and can be arbitrarily deformed to fit the shape of the defect site, while releasing bioactive ions that promote bone regeneration.^{8,9} Unfortunately, current research on additional biomaterials, such as injectable

¹The First Affiliated Hospital of Hainan Medical University, Haikou, Hainan, China

²Municipal Hospital Affiliated to Medical School of Taizhou University, Taizhou, Zhejiang, China

³The Second Affiliated Hospital of Hainan Medical University, Haikou, Hainan, China

⁴Key Laboratory of Emergency and Trauma of Hainan Medical University, Ministry of Education, Haikou, Hainan, China

⁵School of Pharmaceutical Sciences, Wenzhou Medical University, Wenzhou, Zhejiang, China

Corresponding authors:

Lei Peng, The First Affiliated Hospital of Hainan Medical University, Longhua Road No. 31, Haikou 570102, Hainan Province, China; Key Laboratory of Emergency and Trauma of Hainan Medical University, Ministry of Education, Xueyuan Road No. 3, Haikou 571199, Hainan Province China.
 Email: xiaobo197518@163.com

Yingzheng Zhao, School of Pharmaceutical Sciences, Wenzhou Medical University, Chashan street, Wenzhou 325035, Zhejiang Province, China.
 Email: pharmtds@163.com



Creative Commons Non Commercial CC BY-NC: This article is distributed under the terms of the Creative Commons

Attribution-NonCommercial 4.0 License (<https://creativecommons.org/licenses/by-nc/4.0/>) which permits non-commercial use, reproduction and distribution of the work without further permission provided the original work is attributed as specified on the SAGE and Open Access pages (<https://us.sagepub.com/en-us/nam/open-access-at-sage>).

PLGA microspheres, nanocomposite hydrogels, double-network hydrogels, silk fibroin/hydroxyapatite scaffolds, and silk fibroin/carboxymethyl chitosan nanocrystal scaffolds, indicates that these biomaterials suffer from rapid degradation, fast release of drugs, low mechanical strength or local gas and acidic metabolites.^{10–13} Therefore, efforts are being made to address the above challenges with traditional biomaterials.

An ideal bone repair scaffold must have a structure and composition similar to natural bone with biocompatibility, high mechanical properties, and suitable degradability.^{14–16} Silk fiber (F), a tough and filamentous fiber, is obtained after silkworm cocoon degumming. Silk fibroin (SF), a natural macromolecular protein, is obtained by dissolving and purifying the fiber by lithium bromide. Due to its biocompatibility, biodegradability and ease of manufacture, SF has been considered a potential biomaterial carrier for tissue regeneration.¹⁷ However, weak mechanical properties and poor osteoinductivity and osteoconductivity have limited the application of SF in bone tissue engineering.^{18,19} Hydroxyapatite (HAp), the main component of bone inorganic phase, is biocompatible without any inflammation problem, which has been widely studied as a bone substitute for its high bone osteoconductive properties²⁰ and bone regeneration ability.^{21,22} There have been many studies on biomaterials combining SF and HAp in the regeneration of bone defects, and these materials have been indicated to enhance stereoscopic conformation, osteoconductivity and surface roughness, which are conducive to the adhesion and differentiation of BMSCs.^{23–25}

Magnesium is one of the indispensable elements of an organism and is involved in many physiological activities. It can prevent osteoporosis, regulate immune function, and play a protective role in the nervous system. Not surprisingly, 50% of the body's magnesium is stored in bone.²⁶ Moreover, Mg plays an important role in promoting the formation of HAp crystals, mineral calcification deposition, and increasing bone cell adhesion, proliferation and differentiation.^{27,28} It could also enhance bone tissue growth and promote local blood perfusion.²⁹ However, high Mg ions levels could inhibit osteoblast activity and cause bone disease.³⁰ Pure magnesium has been limited in terms of research and clinical applications in orthopaedics because of its fast degradation under physiological conditions, releasing hydrogen gas into the surrounding fluid environment.³¹ To address this problem, here, nanometer magnesia (MgO)^{32,33} were dispersed within multi-layer porous 3D scaffolds composed of SF and F. MgO is odourless, non-toxic, small in particle size, large in specific surface area, and high in hardness. It is an alkaline oxide that combines with water to form magnesium hydroxide under certain conditions, which are slightly alkaline. The pH, a common physical and chemical characteristic of the microenvironment around scaffold materials surfaces, can affect the survival state of BMSCs directly. It has been reported that the local microenvironment formed by biomaterials plays an

important role in the behavior of bone cells and thus affects the formation of new bone.³⁴ An acidic extracellular microenvironment is one of the factors that results in tumors or inflammatory responses of cells.³⁵ Nevertheless, some studies have demonstrated that a weak alkaline microenvironment can stimulate osteoblast differentiation while suppressing osteoclast generation and promoting osteoblast survival to promote the nucleation of apatite.^{36,37} With an increase in pH from 7.4 to 8.5, the activity of alkaline phosphatase (ALP) can be improved significantly.^{38,39} The weak alkaline microenvironment created by biomaterials may be an effective strategy to improve osteogenic activity and markers of osteoblast differentiation.

In this study, the SF internal structure is crosslinked by ultrasonication to form a gel, and F with a network structure can provide a skeleton or condensation nuclei. MgO is selected to be embedded in an SF/F 3D scaffold because MgO can release magnesium ions and create a local weak alkaline micro-environment. With the increased or decreased MgO content, the alkalinity range of the scaffold will change accordingly. As a reflection of potential biological activity, mineralized HAp usually deposit on the interior and surface of SF/F/MgO scaffold⁴⁰ in a bio-inspired fashion, which can significantly improve the mechanical properties of the scaffold. MgO and HAp are encapsulated inside the scaffold, and this structure further realizes the slow release of MgO. Therefore, a suitable magnesium ion release concentration and weak alkaline microenvironment are guaranteed. The scaffold is evaluated *in vitro* regarding its physical and chemical properties. Then, the adhesion, proliferation and differentiation of SD rat BMSCs are evaluated. At last, the scaffold is tested *in vivo* for a femoral defect model in SD rats, and bone regeneration is evaluated 4, 6 and 8 weeks after implantation. The results *in vitro* and *in vivo* showed that SFFHM scaffold has unique physicochemical and biological properties, and it can trigger osteogenic differentiation and accelerate bone regeneration. The purpose of this work is to fabricate a 3D multi-functional bone regeneration scaffolds using simple methods (consisting of silk fibroin, silk fiber, hydroxyapatite and nano magnesium oxide) with beneficial properties of each individual added component, providing a superior scaffold for bone tissue engineering. The composition of each type of scaffold is shown in Table 1; the entire preparation and application strategy is described in Scheme 1.

Materials and methods

Preparation of silk fibers and silk fibroin

Silk fibroin was obtained from *bombyx mori* silk cocoons sourced from HaiNan Medical University (Hainan, China) following a previously reported protocol.⁴¹ Briefly, 10 g silkworm cocoons was cut into pieces and added to 2.0 L boiling aqueous solution of 0.02 M sodium carbonate

(Na_2CO_3) (Sigma-Aldrich) to remove sericin for 1 h, and new Na_2CO_3 solution was added gradually as it boiled. Silk fibers were obtained after being thoroughly rinsed with deionized water and dried completely in a 65°C oven. The degummed silk fibers were dissolved in 9.3 M lithium bromide (LiBr, Sigma-Aldrich) solution at 60°C overnight. After that, the solutions were dialyzed with a cellulose dialysis membrane (7000 Mw, Thermo, USA) for 72 h to obtain a pure aqueous silk solution and then centrifuged at 12000 rpm for 15 min to remove impurities. The obtained SF solution was frozen at -80°C for 4–6 h and then lyophilized to obtain an SF sponge.

Fabrication of SFF-HAp-MgO composite scaffolds

To synthesize the SFF/HAp/MgO (SFFHM) scaffold, MgO (≤ 50 nm particle size, Sigma-Aldrich, USA) at different (0, 1, 3, and 5) wt.% and 3 wt.% silk fibers were

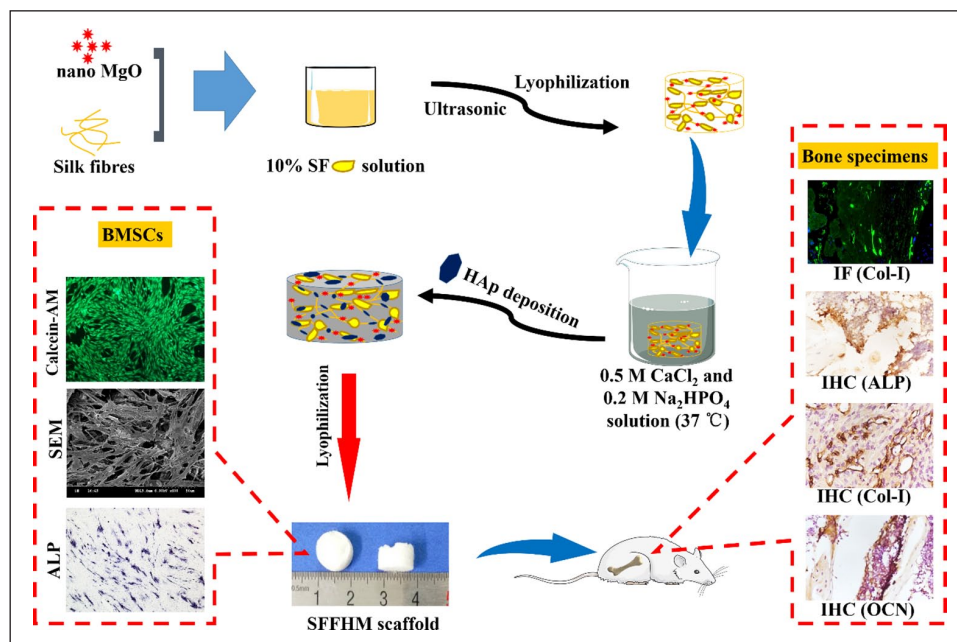
blended to normal saline solution containing 10 wt.% SF and stirring continuously. After mixing evenly, the SF was cross-linked by ultrasonication for 60 seconds, and the power was 150 watts. The resulting crosslinked mixture was transferred into a 48-well plate and frozen at -80°C for 24 h followed by vacuum freeze-drying for 36 h. The HAp were gradually deposited in the as-prepared scaffolds by stirring evenly in the mineralized solution which consisted of 0.5 M CaCl_2 (Solarbio, English) and 0.2 M Na_2HPO_4 (Solarbio, English) for 6 h at 37°C . The wet composite scaffolds were frozen at -80°C for 24 h, followed by lyophilization again. Other groups scaffolds were synthesized by following the above procedure without the addition of corresponding ingredients. Finally, the prepared composite scaffolds were sealed with silicone desiccant. (According to the cell activity test results below of the composite scaffolds with different contents of MgO, we selected 1 wt.% MgO in the composite scaffold as the optimal ratio, which was used in all other experiments of this manuscript).

Table I. Abbreviations of different samples and the descriptions of corresponding composition.

Name of samples	Descriptions of corresponding composition
SF	Silk fibroin lyophilized scaffold
SFF	Original scaffold of SF with silk fiber
SFFH	Original scaffold with HAp deposition
SFFM	Original scaffold with nano MgO incorporation
SFFHM	Original scaffold with HAp and nano MgO incorporation

Surface morphology and conformation properties

Scanning electron microscopy (SEM; Hitachi, H-7500, Japan) was used to evaluate the surface morphology and architecture of composite scaffolds. Briefly, cross-sectioned scaffolds after lyophilization were sputter-coated with gold. The samples were imaged at an operating voltage of 5.0 kV. Fourier Transform Infrared (FTIR; Nicolet, Madison, WI) analysis was used to evaluate the protein



Scheme 1. Schematic illustration of the SFFHM scaffold preparation, the effects on BMSCs and the expression of related markers in situ new bone tissue.

secondary conformation, sample purity and the effect of HAp on sample conformation in the range from 4000 cm⁻¹ to 400 cm⁻¹.

Porosity and swelling estimation

The porosity of all scaffolds, which were cut into equal volumes (10 mm diameter × 5 mm height), was evaluated by using a liquid displacement method.⁴² Briefly, the prepared dry scaffolds were placed in a determined volume (V1) of ethanol for 10 min for voids to be filled completely. The volume was recorded V2 after scaffold immersion. After scaffold removal, the remaining volume of ethanol was noted as V3. Porosity was calculated according to the following equation:

$$\text{Scaffold Porosity (\%)} = \left[\frac{(V1-V3)}{(V2-V3)} \right] \times 100$$

The water retention ability of scaffolds was evaluated using a conventional gravimetric procedure. The lyophilized scaffolds were weighed and recorded (W_i) followed by immersion in phosphate buffered saline (PBS, pH = 7.2, Gibco). At the predetermined time points, scaffolds were carefully removed, the surface water was wiped with filter paper, and the swollen weight (W_s) was recorded. The swelling ratio was calculated using the equation:

$$\text{Swelling Ratio (\%)} = (W_s - W_i) / W_i \times 100$$

Alkalinity measurements

To measure the pH of the microenvironment surrounding samples surfaces, samples (0.05 g each) were immersed with 5 ml of PBS (pH 7.2) for various times at 37°C in 15 ml centrifuge tubes. Then, at each time point, specifically 0, 3, 8, 12, 24, 48, 72, 120 and 168 h, the pH of the PBS immersion sample was measured via a pH meter (FE28-FiveEasy Plus, METTLER TOLEDO, Switzerland). Before each measurement, the solution was shaken to be homogeneous, and the pH meter probe was placed approximately 3 mm above the sample surface. In addition, throughout the pH measurement, the centrifuge tubes with samples and liquid were never moved. Three parallel samples were detected to ensure the accuracy of the data.

In vitro degradation and Mg ions test

The degradation of the composite scaffolds were evaluated by following procedure: Briefly, the scaffolds were immersed in 5 ml PBS (pH 7.2) containing 2 U/ml protease XIV derived from *Streptomyces griseus* with an activity of 3.5 U/mg (Sigma-Aldrich, USA) and incubated at 37°C.⁴³ Enzyme solution was replaced at each time point with freshly prepared solution. All samples were equally weighed (0.05 g), and the initial weight was recorded as W₀. After each incubation period, the scaffolds were put in

an oven to dry. The dry weights of each sample were noted as (W_d). The degradation percentage of weight remaining was calculated by using the following equation:

$$\text{Weight remaining (\%)} = (W_d / W_0) \times 100$$

2 mL degradation solution was collected for each samples at 0, 3, 7, 14, 21, 28, and 42 days, and fresh enzyme-containing solution (2 mL) was replenished. The release of Mg ions was determined by inductively coupled plasma mass spectrometry (ICP, Agilent 710, California, USA). The typical standard curves for Mg ions were constructed by using known Mg ion contents for reference. This curve was used to calculate the amount and cumulative amount of Mg ions released at each time point. Three parallel measurements of each group were conducted for averaging.

Mechanical properties

The mechanical properties of scaffolds were studied using a Universal Testing Machine (UTM, Instron 3343, USA) fitted with a 1000 N load cell. Compression tests of the spare freeze-dried scaffolds samples were conducted at room temperature. For recording, displacement control mode was used with a crosshead displacement rate of 2 mm/min until the deformation reached 95% of the sample following the ASTM standard for compressive properties of rigid cellular plastics. The compressive stress-strain curves were plotted, and the compressive modulus was determined for each sample using Origin 2018 software.

Cell culture

Sprague-Dawley (SD) rat BMSCs, complete medium and the medium for osteogenic induction and differentiation were purchased from Cyagen Biosciences (USA). The cells were maintained in α-modified Eagle's medium (α-MEM) supplemented with 10% foetal bovine serum (FBS), 1% penicillin-streptomycin and 1% glutamine. The cell incubator was maintained at 37°C under saturated humidity with 5% CO₂. Inductive medium, which was used to study osteogenic differentiation, was made from 175 ml culture medium to which 20 ml FBS, 2 ml β-sodium glycerophosphate, 2 ml glutamine, 2 ml penicillin-streptomycin, 400 μl ascorbic acid, and 20 μl dexamethasone were added. Media were refreshed every 2 days in all cases. Before contact with BMSCs, scaffolds of each group were sterilized by exposure to ultraviolet light for 24 h, and the scaffold soaking solution (0.1 g scaffold:1 ml PBS) was filtered through a 0.22 μm microporous membrane.

Cell viability

The BMSCs metabolic activity within scaffold soaking solution (10% of the mixed medium) of SFF/HAp with

MgO at different content (0, 1, 3 and 5) wt.% and PBS (control) was evaluated by 3-(4,5-dimethylthiazol-2-yl)-5-(3,4-diphenyltetrazolium) bromide (MTT, Sigma-Aldrich, USA) assay after 24, 48, and 72 h of cell culture. At each experimental time point, the samples were washed with 1X PBS, and 100 μ L cell medium with MTT solution (5 mg/ml stock in PBS, Sigma-Aldrich, USA) was added and incubated at 37°C and 5% CO₂ for 4 h. Then, 150 μ L dimethyl sulfoxide (DMSO, Sigma Aldrich, USA) was used to replace the medium and to solubilize the formazan crystals, which were oscillated for 10 min at room temperature. The sample absorbance was monitored at 570 nm using a Synergy™ Mx monochromator-based multi-mode microplate reader (Biotek Instruments, Inc., USA).

Furthermore, BMSCs activity was evaluated within different acid-base microenvironments (pH 6.5, 7.0, 7.2–7.4, 8.0, 8.5, 9.0) in medium and the Control group with medium at pH 7.2–7.4 (common medium). As described above, the MTT assay was used to detect the OD value of each group after 24 and 72 h of cell culturing.

BMSCs morphology, adhesion and proliferation study

The morphology and adhesion of BMSCs on the scaffolds were examined by scanning electron microscopy (SEM, Hitachi, Japan). Sterilized scaffolds were cut into thin slices (10 mm diameter and 2 mm thickness), followed by incubation in complete medium for 1 h. BMSCs were seeded on the surface of each sheet at a density of 1×10^5 cells. After 48 h of cell culture, the samples were washed for 1 min with PBS and fixed by the addition of 2.5% glutaraldehyde for 2 h. After being washed three times for 15 min, the samples were dehydrated at increasing concentrations of ethanol solution (30%, 50%, 70%, 80%, 90% and 100%) for 15 min each and then dried. The specimens were fixed on a sample holder for observation after conventional coating with a gold film.

Live and dead cell staining. To visualize cell adhesion and proliferation on scaffolds cut into a 10 mm diameter and 1 mm thickness after culturing for 48 h and 72 h, live cells were stained with Calcein-AM (green), and dead cell nuclei were stained using propidium iodide (PI) (red) according to the manufacturer's instructions. Briefly, 5 μ L Calcein-AM solution (2 mM) and 15 μ L PI solution (1.5 mM) were added to 5 ml $1 \times$ assay buffer and mixed well to prepare working fluid in the dark. After aspirating the medium, 500 μ L working fluid was added per well and incubated at 37°C. Cell proliferation was imaged using a fluorescence microscope (Nikon, Japan), and Image-pro software was used to measure cell spreading and the proliferation area.

BMSCs osteogenic differentiation

To evaluate the osteogenic differentiation of BMSCs in osteogenic differentiation medium containing the scaffold

soaking solution (10% v/v), alizarin red S (ARS) staining, ALP staining, ALP activity and osteocalcin (OCN) immunofluorescence staining were measured.

ARS staining was imparted to examine the presence of mineralized nodules which reflected the extent of mineral deposition during BMSCs culture. When cultivating to 2 weeks, cells were fixed with 4% paraformaldehyde for 30 min and washed three times for 3 min, followed by staining with 1 ml/well ARS staining solution for 10 min at 37°C and imaging using a fluorescence microscope (Nikon, Japan). To take an appropriate amount of samples before and after each use of the mixed culture solution, 10% cetylpyridinium chloride was added to the samples and measure their absorbance (570 nm), and calculating the difference between the absorbance before and after each use. This difference was cumulatively subtracted from raw samples (SFFH and SFFHM) to exclude calcium interference of HAp. The quantitative analysis of deposited calcium nodules was estimated through cetylpyridinium chloride treatment. As before, the absorbance of desorbed calcium ions was measured by a micro-plate spectrophotometer (Thermo Scientific, USA) at 570 nm.

ALP activity was qualitatively estimated by ALP staining. BMSCs were seeded in 6-well cell-culture plates at a density of 1×10^5 cells/mL. After 7 d and 14 d of culture, cells were fixed in 70% ethanol, and a BCIP/NBT alkaline phosphatase reagent kit was used according to the manufacturer's instructions. Under alkaline phosphatase catalysis, BCIP is hydrolyzed to produce a highly reactive product that will react with NBT to form insoluble dark blue to bluish-purple NBT-formazan. The bluer and greater the product is, the higher the activity of alkaline phosphatase, and vice versa. Image-pro software was used to measure the colored areas of ALP.

In addition, for quantitative analysis of ALP activity, the cell culture programme and density were the same as those described above. After 3 d, 7 d and 14 d of culture, the quantitative analysis of ALP activity was determined by using an ALP Assay Kit (Beyotime). The cell culture medium was aspirated and washed twice with PBS, 200 μ L of cell lysis buffer for Western and IP without inhibitors (Beyotime) was added to each well, and the cells were lysed at 4°C for 15 min. Then, all lysis buffers with lysed cell were centrifuged at 4°C, and supernatants were collected and reacted with para-nitrophenyl phosphate (pNPP, Beyotime) for 30 min at 37°C to generate p-nitrophenol. At the end of the reaction, the concentrations of p-nitrophenol (c(p-nitrophenol)) were measured by an enzyme-labelling instrument at 405 nm. The total protein amount (c(total proteins)) of the cell lysate was determined by the BCA protein assay method. The quantitative results of alkaline phosphatase activity were calculated by c(p-nitrophenol):c(total proteins), and the obtained data were normalized to the blank control data to obtain the relative ALP activity data of each group.

OCN protein, a specific marker of osteogenic differentiation, was examined using immunofluorescence staining. After 21 d, the BMSCs were fixed with 4% paraformaldehyde for 10 min at room temperature. After washing with PBS 3 times and incubating with 0.5% Triton X-100 (Sigma-Aldrich) for 15 min, the cells were incubated with 5% bovine serum albumin (BSA, Genaray, Shanghai, China) for 1 h at 37°C in an incubator and then with primary mouse monoclonal OCN antibody (1:200 dilutions) overnight at 4°C, followed by incubation with Alexa Fluor488-conjugated donkey polyclonal secondary antibody to mouse (1:1000, Abcam, Cambridge, MA). Finally, the nuclei were stained with 4',6-diamidino-2-phenylindole (DAPI; Solarbio, China) and fixed on a glass slide in the dark. The slides were observed by a fluorescence microscope (Nikon, Japan). Quantitative analysis of OCN protein expression was performed using ImageJ software.

SD rat femoral defect model

The male SD rats with a weight of approximately 200 g were supplied by the Animal Experiment Center of Hai Nan Medical University in compliance with all regulatory guidelines. These rats were randomly divided into five groups of 10 rats each (total 50 animals), and anaesthetised by intraperitoneal injection of chloral hydrate (0.3 ml/100 g). After the right legs were shaved and sterilized, surgical incision and bone exposure were performed around the lateral epicondyle on femurs, and a defect 3 mm in diameter and 3 mm in depth was created using a hand-drill under continuous saline buffer irrigation. Thereafter, scaffolds in each group that were cut into a suitable shape were implanted into the prepared holes. For the blank control group, the same defects were created without any treatment, and the wound was sutured layer by layer. The animals were free to obtain water and food after surgery. All animal procedures were approved by the Animal Ethics Committee of Hainan Medical University.

Micro computed tomography (micro-CT) scanning analysis

After scaffold implantation for 4, 6, and 8 weeks, five SD rats per group at each time point were scanned by a micro-CT system (Skyscan1176, Bruker, Germany). The scanning parameters were set at an energy source of 70 kV and 110 μ A using Al 1mm filter with a spatial resolution of 18 μ m. A cylinder region of interest (ROI) of 3 mm in diameter and depth at the bone defect area was selected and reconstructed by a CT-analyser. Ninety axial images within a range of 3 mm depth were reconstructed into a 3D image with grey threshold of 50–255, and 2D slice analysis was conducted in Data Viewer (Skyscan Germany). Thereafter, the bone tissue volume density (BV/TV, %), bone mineral density (BMD, mg/cm³), and trabecular

number (Tb.N, mm⁻¹) in the ROI of bone tunnel were evaluated in the CTAn program (Skyscan, Germany).

Histological analysis

At 4 and 8 weeks post-operation, five SD rats per group were sacrificed respectively by overdose anesthesia, and the right femurs were collected and fixed in 4% phosphate-buffered paraformaldehyde solution for 48 h. The retrieved rat femurs of each group were processed for histological analysis. Briefly, the specimens were decalcified in ethylenediaminetetraacetic acid (EDTA). After dehydration in a graded ethanol series, the specimens were cleared in xylene and embedded in paraffin. Then, the paraffin was cut into 7 μ m thick microsections for routine histological assessments with haematoxylin and eosin (H&E) (Solarbio, English) and Masson's trichrome staining (MTS) (Solarbio, English). Immunofluorescence staining for Col-I and immunohistochemical staining for ALP, collagen-I (Col-I) and OCN were performed for histological examination, and the sections were analyzed under an optical microscope (Nikon ECLIPSE 80i, Japan). The primary antibodies were anti-Col-I (Abcam, USA, ab34710), anti-ALP (Abcam, USA, ab95462) and anti-OCN (Abcam, USA, ab13420). Quantitative analysis of the expression of the above indicators was performed using Image-pro software.

Statistical analysis

All experiments were performed at least in triplicate, and data represented the mean \pm standard deviation unless otherwise stated. Data were statistically processed using one way analysis of variance (ANOVA) to assess significant differences amongst various groups followed with a Tukey test. $p < 0.05$ was considered significant, $p < 0.01$ was considered highly significant.

Results

Morphological analysis and conformation characteristics

Figure 1(a) to (e) shows the typical SEM images of the composite scaffolds and their corresponding components. SEM images revealed irregular porous and interconnected cubical structure within scaffolds. Compared to the pure SF scaffolds, the SFF scaffolds demonstrated more compact pore-like structures, as adding silk fibers provides a bracket structure for the material internal space. It is worth noting that adding MgO does not affect the smooth morphology of SFF scaffolds, which further confirms uniform blending of MgO in the scaffolds, but the porosity decreases somewhat. The addition of HAp to the SFF scaffolds or the simultaneous addition of MgO reduced the porosity of the material, and the surface morphology became slightly rough.

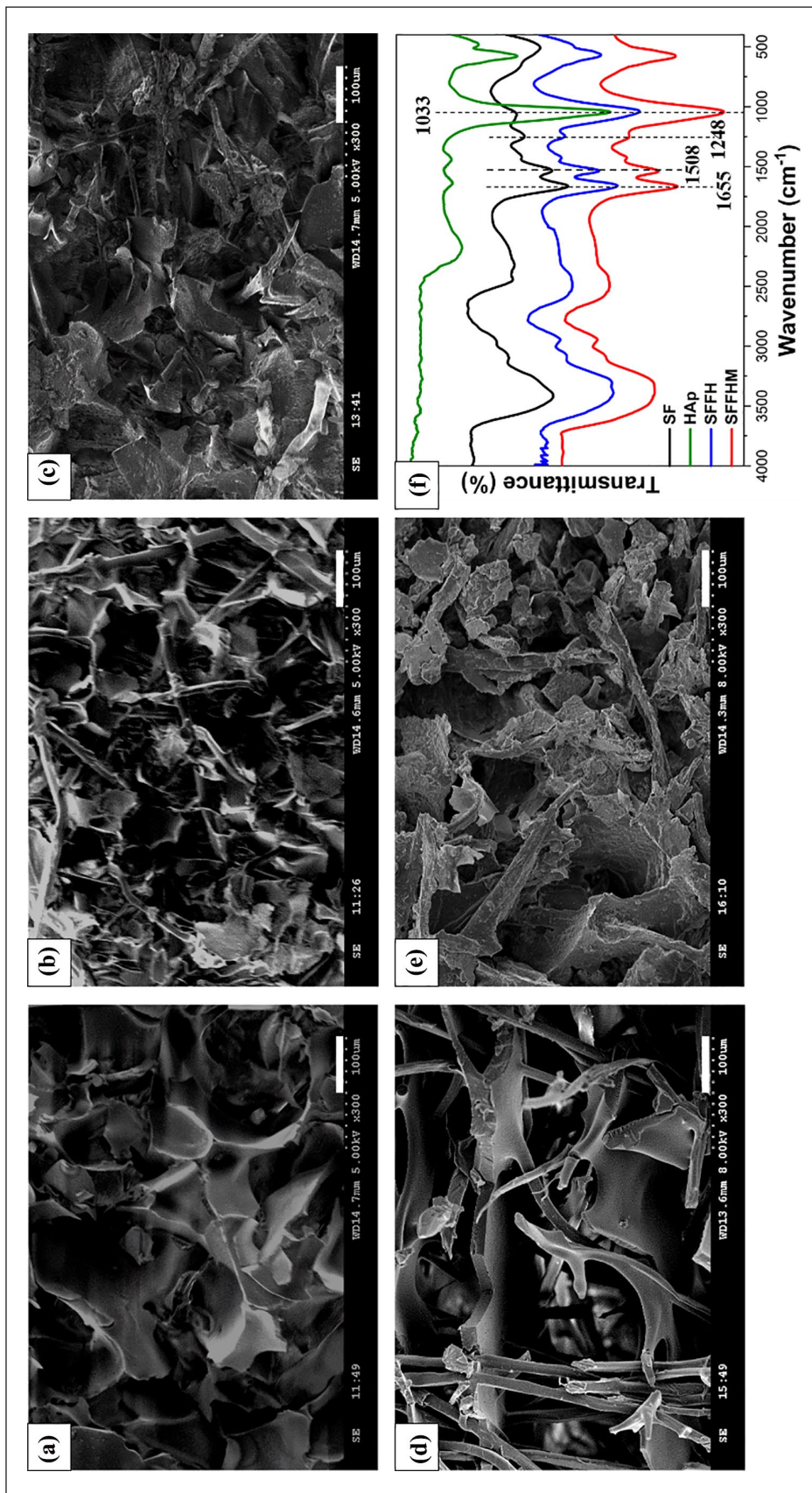


Figure 1. Scanning electron microscopy (SEM) images of composite scaffolds exhibiting porous morphology and fiber network structure. (a) Silk fibroin-silk fiber scaffold. (b) Silk fibroin-silk fiber scaffold. (c) Silk fibroin-silk fiber-HAp scaffold. (d) Silk fibroin-silk fiber-MgO scaffold. (e) Silk fibroin-silk fiber-HAp-MgO scaffold. (Scale bar: 50 μm). (f) FTIR spectra of silk fibroin, HAp, silk fibroin-silk fiber-HAp and silk fibroin-silk fiber-HAp-MgO.

Further, the protein secondary conformation and the effect of HAp addition on sample conformation were evaluated by FTIR spectroscopy. Pure silk fibroin as well as all the composite scaffolds showed adsorption bands at approximately 1655 cm^{-1} (amide I) and 1508 cm^{-1} (amide II), and the shoulder at 1248 cm^{-1} confirmed the β -sheet is the main secondary conformation (Figure 1(f)). The peaks at 1033 cm^{-1} were assigned to P-O bending of phosphate group (PO_4^{3-}), suggesting the existence of HAp, and the intensity decreased seriously with the incorporation of SF/F owing to HAp adsorption on the scaffolds surface. However, the addition of MgO micro particles did not cause structural conformation modifications to SFFHM.

Porosity and water retention ability of scaffolds

Some researchers reported that the porosity ranges between 40 and 90% for various biomaterials, promoting bone cell adhesion of the implant and osteoinduction.⁴⁴ The porosity of scaffold is proportional to the surface area. Therefore, designing scaffolds provides a large surface area leading to cellular attachment, growth and proliferation.⁴⁵ The average porosities of SF, SFF, SFFH, SFFM and SFFHM were calculated to be 93.05 ± 2.71 , 84.87 ± 10.00 , 58.95 ± 7.64 , 71.51 ± 12.24 and $57.28 \pm 8.30\%$, respectively (Figure 2(a)). We observed that the porosity of SFFH and SFFHM scaffolds were demonstrated a decrease, owing to the fact that HAp and MgO were deposited on the surface of SF and in the F grid, however, the porosity of the two was similar. In turn, the slow release of HAp and MgO can further increase the porosity of the scaffolds with the degradation of SFF.

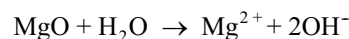
The SFFHM composite scaffold showed a significantly reduced swelling ratio when immersed in PBS (pH 7.2) relative to pure SF and other groups without HAp or MgO, or neither. The scaffolds swelled gradually and reached equilibrium in approximately 50 min after immersion in PBS. The swelling ratios of the pure SF scaffolds without HAp deposition and MgO were nearly 1.6 times those of the SFFHM scaffolds (Figure 2(b)). Moreover, other scaffolds with fiber reinforcement (SFF, SFFH, SFFM) showed lesser swelling compared to the pure silk fibroin scaffolds. These results indicate that the larger the porosity, the greater the swelling rate, and vice versa.

Alkalinity of the microenvironment

The pH values of solutions used to immerse various samples for 0, 3, 8, 12, 24, 48, 72, 120, and 168 h were measured, and the results are shown in Figure 2(c). The initial pH value of all groups was approximately 7.2. After 3 h of soaking at 37°C , the pH values of SF, SFF and SFFH groups were slightly decreased to 6.86, 6.93 and 6.97, respectively. However, the pH values of the SFFM and SFFHM groups increased to 7.45 and 7.41, respectively. With prolonging the time to 24 h, the pH value of the SF

group changed to 6.87, and the pH values of the SFF and SFFH groups slightly decreased to 6.91 and 6.96, respectively, while the pH value of the SFFM groups sharply reached the peak of 8.36, and the SFFHM groups reached 7.94 with a subsequent peak of 7.94 at 48 h. The pH values of the SFFM and SFFHM groups decreased to 7.37 and 7.69 after 72 h, respectively, and then the pH slowly changed. Nevertheless, the pH values of the SF, SFF and SFFH groups fluctuated smoothly in the ranges of 6.77–6.79, 6.66–6.83 and 6.72–6.87 after 24 h, respectively. The difference is likely resulted from the different dissolution rates of various samples. The decrease in the pH value of each group may be due to the dissociation of glycine (Gly), alanine (Ala) and serine (Ser) after the SF of the scaffolds was dissolved. For SFFM and SFFHM samples, along with the reactions below, the OH^- accumulated on the sample surface, increasing the local alkalinity. Compared with SFFM, there was lower porosity on the SFFHM sample surface, which resulted in fewer active sites to react with H_2O . Therefore, more hydroxyl ions would accumulate on the SFFM surface, leading to faster and stronger alkalinity in the early stage. However, the alkalinity of SFFHM can maintain a stable state for a long time without sudden release.

Reaction formula of MgO in PBS:



According to the above results and analysis, we can conclude that different pH microenvironments can be generated around various sample surfaces. However, the alkaline microenvironments of SFFHM scaffolds would be better for cell activity than those of SFFM scaffolds.

Degradation behaviors and Mg^{2+} release

The degradation of composite scaffolds was determined in PBS with protease XIV. Protease XIV enzyme is known to degrade fibroin crystalline structure.⁴⁶ It was observed that SF scaffold degraded more than 50% of its original weight in 14 days, followed by SFF, SFFM, SFFH and SFFHM scaffolds (Figure 2(d)). The fasted degradation rates of all scaffolds were within 14–21 d. However, SFFH and SFFHM degraded to below average at 35% at 42 d. The results indicated slowing down of the degradation rate following fiber reinforcement and HAp deposition within silk scaffolds. The rate of degradation is related to the porosity caused by silk fiber and HAp addition. Therefore, the degradation rate could possibly be tuned by manipulating the amount of HAp deposition and silk fibers used as reinforcement.

During degradation in vitro, Mg ions were released from composite scaffolds. Theoretically, the total Mg ions concentration of completely dissociated MgO for the 0.05 g scaffold (containing 1 wt.% MgO) soaked in 5 ml PBS with enzyme is $60\text{ }\mu\text{g/ml}$. In general, the Mg ion accumulation of SFFM and SFFHM increased in each group in

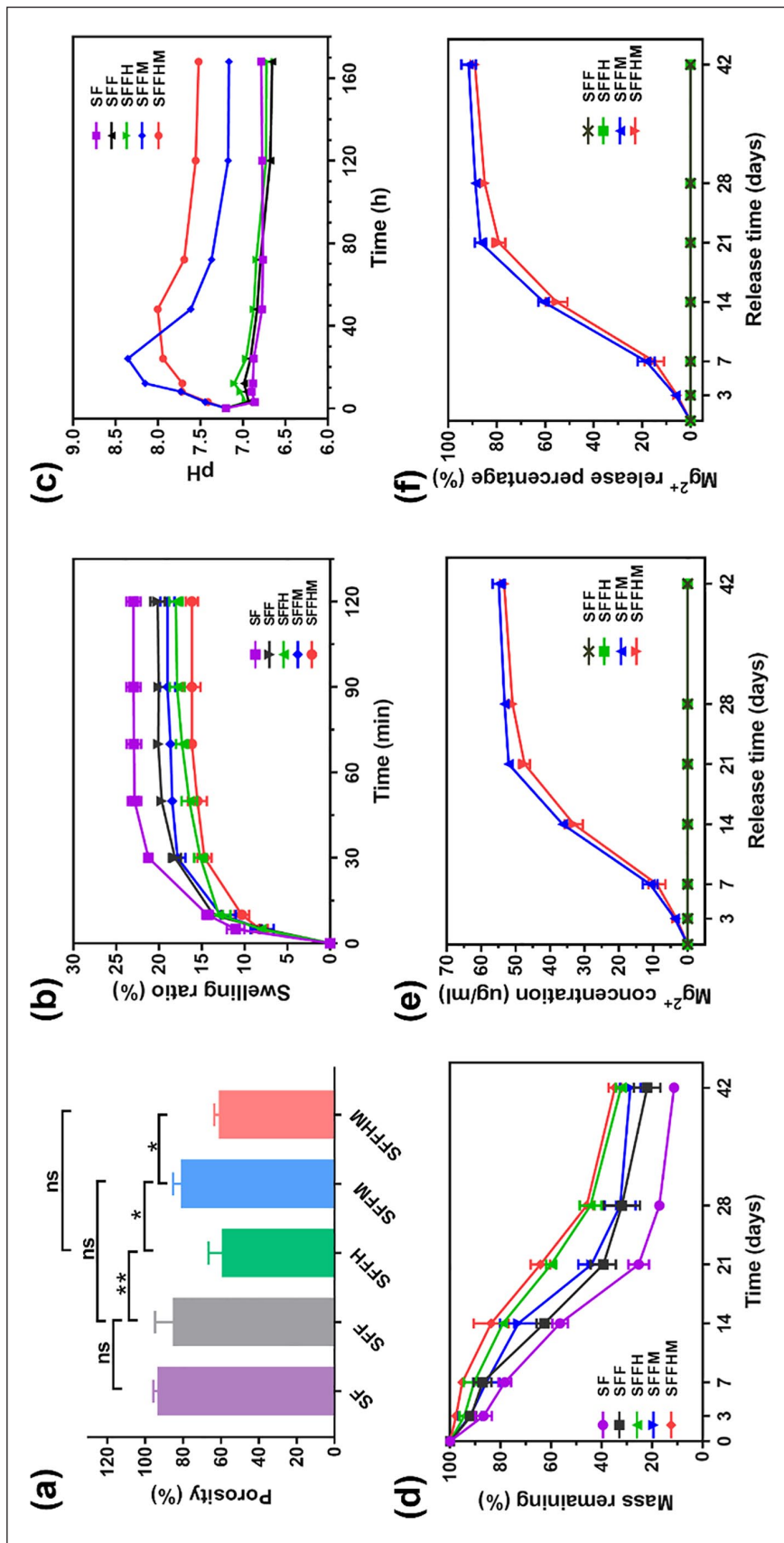


Figure 2. Characterizations of scaffolds. (a) Porosity and (b) Water retention capability of various scaffolds. (c) pH value of PBS solution after immersing samples for various time point. (d) Degradation profile of various scaffolds. (e) Cumulative release concentration and (f) Cumulative release percentage of Mg ions. (** $p < 0.05$, *** $p < 0.01$, ns = not significant, $n = 5$).

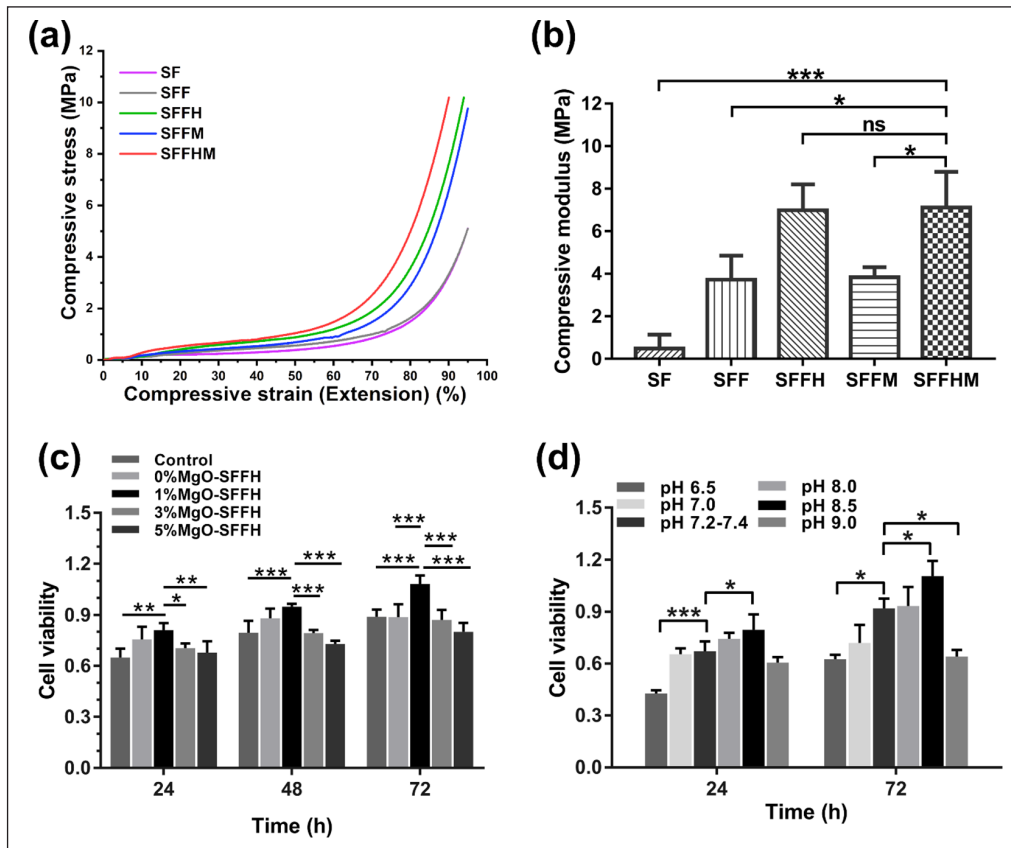


Figure 3. Mechanical properties and cell viability of scaffolds. (a) Graph representing compressive stress-strain curves of various silk scaffolds. (b) Compressive modulus. (c) Cell viability of BMSCs cultured in complete medium and in scaffold soaking solution with MgO at different concentrations. (d) Cell viability of BMSCs cultured in complete medium at different pH values. (* $p < 0.05$, ** $p < 0.01$, *** $p < 0.001$, ns = not significant, $n = 5$).

the degradation medium over time (Figure 2(e) and (f)). The Mg ion concentrations of SFF and SFFH that were not mixed with MgO were maintained at $0 \mu\text{g/ml}$ for 0–42 d. The Mg ions were released from the two scaffolds (SFFM and SFFHM) at 7–21 d relatively faster than at the other time points, and the initial rapid responsive releases were also more significant. This trend was consistent with the degradation rates of the two scaffolds. From week 3, the release of remaining Mg in the scaffolds became stable and reached a sustained rate. The cumulative Mg release from SFFM scaffold into the degradation media within 6 weeks reached approximately 92%, while 89% was released from SFFHM. It also showed that both scaffolds could release Mg ions for at least 6 weeks. The addition of HAp delayed the release of Mg ions to some extent, however, they showed the same release trend.

Mechanical properties

Mechanical properties of scaffolds portray a crucial role in bone tissue engineering applications as adequate compressive strength is required by the grafts for the replacement tissue. Figure 3(a) shows the mechanical characteristics of SF, SFF, SFFH, SFFM and SFFHM scaffolds. The stress

strain curves displayed an initial linear elastic region representing the lower modulus followed by a plateau corresponding to pore wall contortion and consequently a steep increase in stress, suggesting sample flattening. From the results, both fiber reinforcement and HAp incorporation resulted in increased modulus and compressive strength. In addition to SFFH scaffolds, the SFFHM samples showed significantly higher compressive strength and modulus compared to SF, SFF and SFFM. The calculated compressive modulus was $0.49 \pm 0.66 \text{ MPa}$, $3.73 \pm 1.13 \text{ MPa}$, $6.98 \pm 1.22 \text{ MPa}$, $3.83 \pm 0.49 \text{ MPa}$, and $7.11 \pm 1.69 \text{ MPa}$ for SF, SFF, SFFH, SFFM and SFFHM, respectively (Figure 3(b)). The composite scaffold SFFHM showed a maximum compressive modulus (approximately 15-fold higher) in comparison to the pure SF scaffolds. The increasing trends of compressive strength and modulus were observed for each scaffold type with the following trend: $\text{SF} < \text{SFF} \leq \text{SFFM} < \text{SFFH} \leq \text{SFFHM}$ ($p < 0.05$).

Cell viability assay

Preliminarily, we have examined the effect of material on BMSCs to screen the appropriate MgO content in the composite scaffold by MTT assay after culturing the BMSCs

within scaffold soaking solution with MgO at various concentrations for 24, 48, and 72 h. As shown in Figure 3(c), interestingly, the SFFHM scaffold showed a decrease in the cell proliferation with an increase in the MgO weight percentage; however, the SFFHM with 1 wt.% MgO showed the highest BMSCs proliferation at each time point. This indicates the MgO is a vital component of the scaffold that can both serve as a stimulator, encouraging better growth and proliferation of BMSCs, and as an inhibitor of cell proliferation at a high concentration. We hypothesize that this result is closely related to the Mg ions and alkaline microenvironment released by the scaffold, and the high pH alkaline microenvironment of high-proportioned MgO can inhibit the proliferation of BMSCs.

Further, the MTT assay was used to investigate the BMSCs growth and proliferation effects of different gradient acid-base microenvironments, and the results are shown in Figure 3(d). After culture for 24 h, compared with the pH 7.2–7.4 group (control group), the BMSC cells in pH 8.5 complete medium showed significantly high OD values; however, the control group OD values were significantly higher than the pH 6.5 group, and there was no obvious difference among pH 7.0, pH 8.0 and pH 9.0. At 72 h, the proliferation of BMSCs presented a similar trend as that at 24 h, but cell proliferation was inhibited at pH 9.0. The results indicated that the medium at pH 7.2–8.5 could promote the proliferation of BMSCs and that the medium with pH < 6.5 and pH > 8.5 inhibited the proliferation of BMSC cells.

BMSCs adhesion, proliferation and morphology study

To verify the assumption that scaffolds establish a favorable microenvironment for cell survival, live-dead staining was conducted to assess the biocompatibility of these scaffolds. As shown in Figure 4(a) and (b), the variation tendencies of cell density observed in live-dead cell staining fluorescence images, and Figure 4(c) and (d) are the corresponding quantitative analyses of the live cell areas of each pixel at 48 and 72 h. We observe living cells (green) that proliferated significantly when growing in soaking solution of the scaffolds (SFFH, SFFM and SFFHM), and the number of cells has a time-dependent increase, especially SFFHM scaffold. However, the dead cells (red) are hardly visible, indicating that all scaffolds have no obvious toxicity for BMSCs. This trend may be due to the effect of weak alkaline microenvironment and Mg ions created by MgO. The SFFHM composite scaffold supported maximum cell proliferation for BMSCs at both 48 h and 72 h ($p < 0.001$).

Cell attachment is the first step of the interaction between cells and materials, which exerts direct regulation on the following cell behaviors.⁴⁷ SEM was used to detect cell adhesion on various scaffolds. As illustrated in Figure 4(e), BMSCs cultured on the SFF and SFFH for 48 h

exhibited lower cell density. Obviously, an increase in BMSCs density was observed on SFFHM scaffolds, the cells were seen as fibroblastic in appearance, with an elongated fusiform morphology and multiple antennas, and microvilli bulges were visible on the cell surface. BMSCs were in good condition on all four types of scaffolds, suggesting that the SFF-based scaffolds were suitable for cell adhesion. It is worth noting that for SFFHM, cells were observed to be more elongated, full and well spread with significant outstretched filopodia extensions and lamellipodia protrusions as shown, indicating that except for the weak alkaline environment and Mg ions of MgO, HAp increased the surface roughness of SF-F, which is more conducive to cell adhesion and proliferation. The results above may be due to the porous structure of the scaffolds and the synergistic effect of HAp and MgO to promote the formation of cell-cell junctions and extracellular matrix (ECM) in the scaffolds pores, facilitating the transfer of essential nutrients and oxygen to cells.⁴⁸

Differentiation of BMSCs

Figure 5(a) and (d) shows alizarin red staining and quantitative of deposited calcium of cells cultured for 2 weeks, the red spot intensity of the Control, SFF and SFFH groups was weaker and some spots were clustered together. However, the SFFM and SFFHM groups appeared to be significantly denser than the other groups. Red spots were connected together and were larger in size with more mineral deposition. A significantly different trend of samples in the staining intensity and the change sequence was in the following order: Control and SFF with minimal coloring, SFFH with moderate coloring, SFFM with higher coloring, and SFFHM with maximum coloring. The maximum stain intensity of SFFHM can be attributed to the synergistic effect of Mg ions and weak alkaline microenvironment provided by MgO along with osteoconductive HAp in the scaffolds. This indicates the relative potential of SFFHM in BMSCs differentiation towards the osteogenic lineage.

As an early marker, ALP activity was evaluated to investigate the effect of scaffolds on the osteogenic differentiation of BMSCs.⁴⁹ Similarly, Mg ions, a weak alkaline microenvironment and HAp enhanced ALP staining intensity in BMSCs, resulting in more ALP protein and deeper coloring in the SFFHM group than the other groups and control group (Figure 5(b) and (e)). Consistent with these changes, the results of the ALP quantitative assay (Figure 5(f)) at 7 and 14 d exhibited a similar trend relative to the trend in ALP staining. However, there were no significant differences in all groups at day 3 due to the short time of cell culture. Compared to the control group, SFFM and SFFHM exhibited higher ALP activity at day 7, while SFFH also revealed higher ALP activity at day 14, and the SFFM and SFFHM groups were dramatically higher than the Control group.

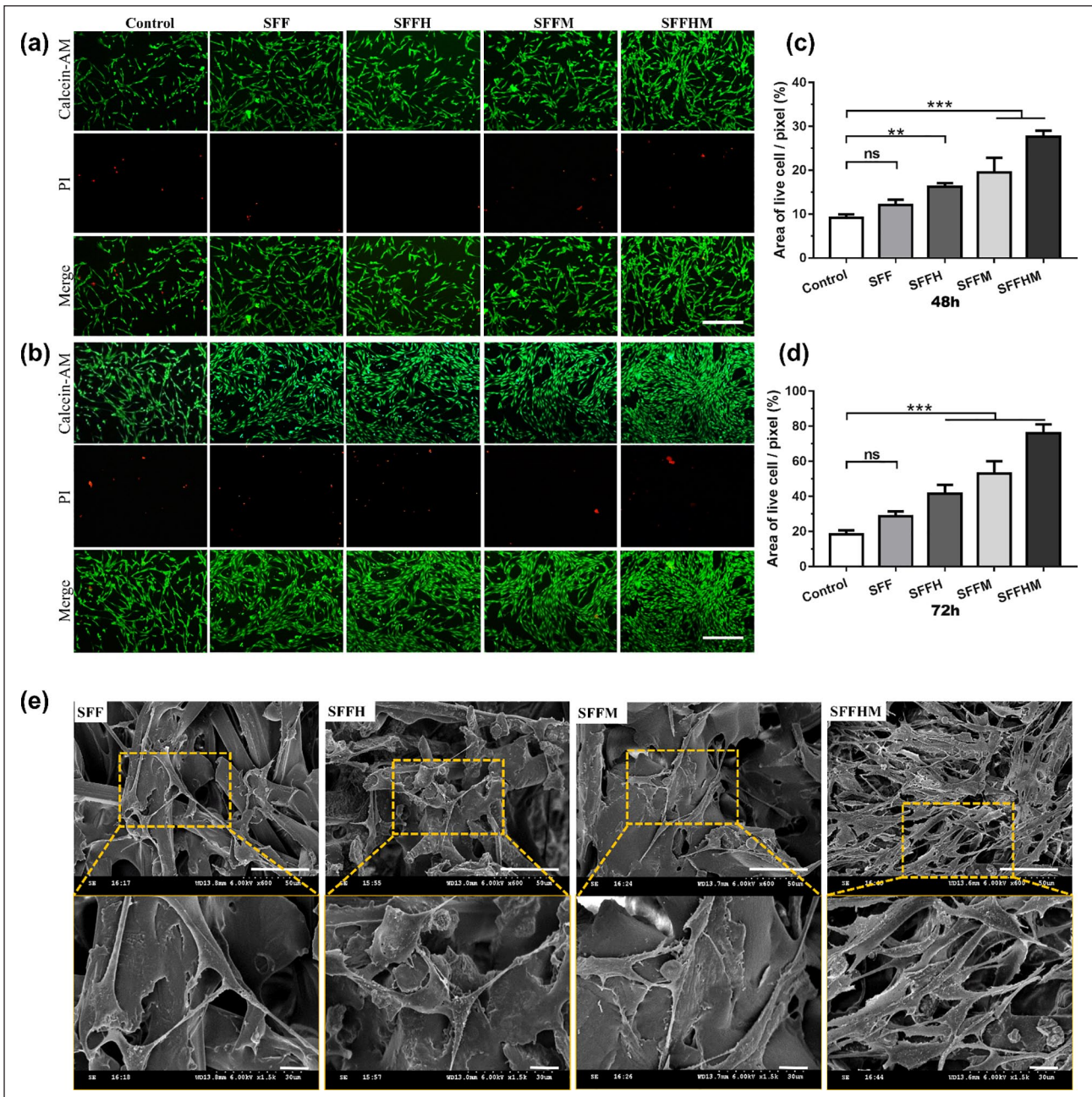


Figure 4. The adhesion, proliferation and morphology of BMSCs: Representative images of Calcein-AM/PI double staining of BMSCs cultured 48 h (a) and 72 h (b), scale bar = 100 μ m (all of a & b), and the corresponding quantitative analysis at (c) 48 h and (d) 72 h. (e) Cell attachment and morphology on the scaffolds after 48 h. The upper and lower rows show typical low-magnification and high-magnification SEM micrographs, respectively. Scale bar: upper row 50 μ m and lower row 10 μ m. (** $p < 0.01$, *** $p < 0.001$, ns = not significant, $n = 3$).

We further evaluated the level of OCN protein expression using immunofluorescence staining. As the results show in Figure 5(c) and (g), the levels of OCN protein expression in the SFF and SFFH groups were similarly low compared to the control group, while the two scaffolds contained MgO exhibited an obvious increase in the OCN content measurements in 21d, when compared to the Control groups; the scaffolds of SFFHM and SFFM showed higher level than the other groups. These results

demonstrated that Mg ions and a weak alkaline microenvironment produced by MgO of scaffolds could obviously induce the osteogenic differentiation of BMSCs.

Micro computed tomography analysis

Silk fibroin composite scaffolds were transplanted in the SD rat femur bone defect model to assess bone tissue distribution and mineralization, while three-dimensional and

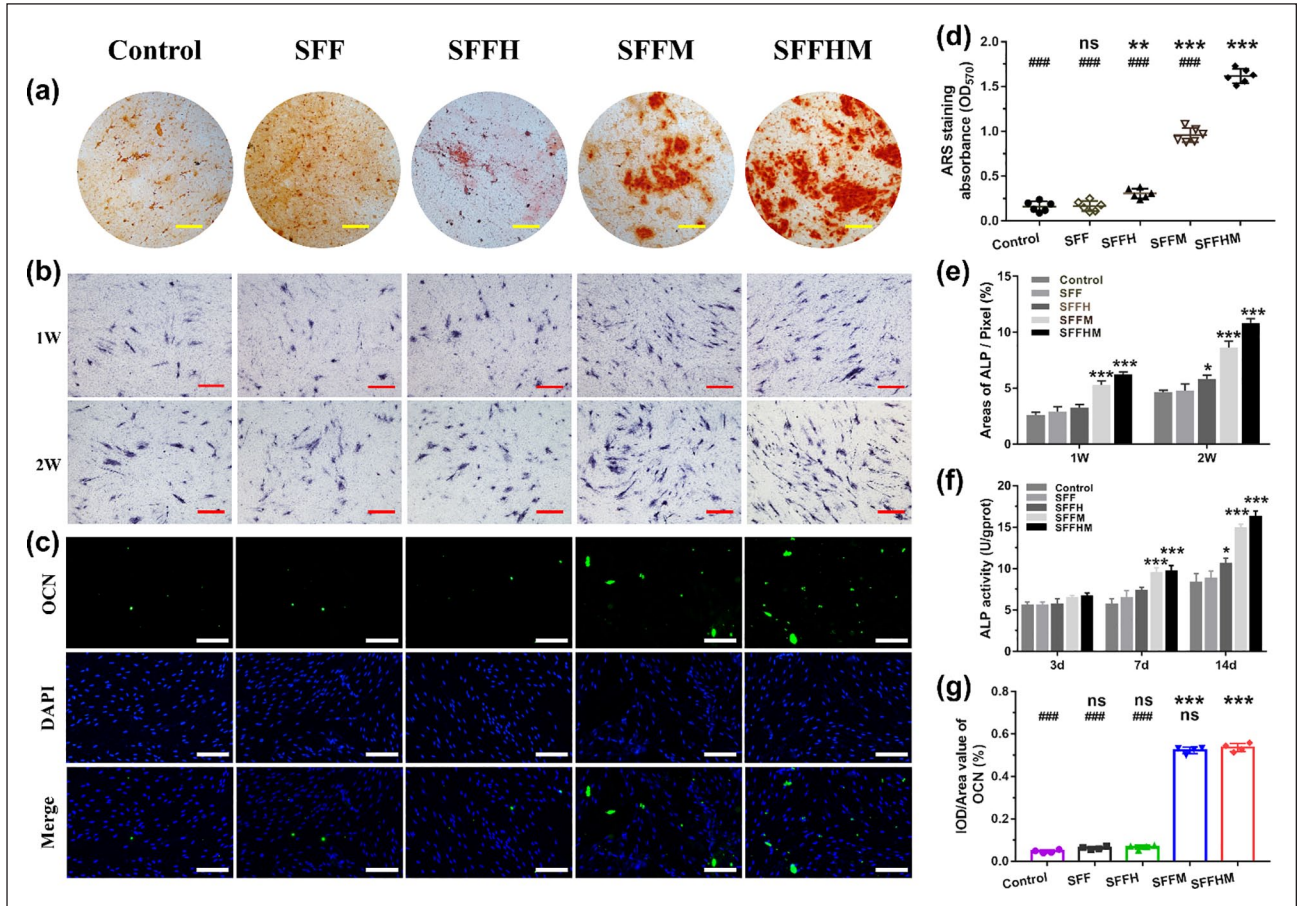


Figure 5. Osteogenesis differentiation of BMSCs in vitro. (a) Alizarin red staining for calcium deposition at 14 d (Scale bar: 200 μ m). (b) ALP staining at week 1 and week 2 (Scale bar: 200 μ m). (c) Immunofluorescence assays for OCN expression at 21 d, with the nucleus stained with DAPI and OCN stained in green (Scale bar: 100 μ m). The corresponding quantitative analysis of Alizarin red staining for calcium deposition (d), ALP at 1 week and 2 weeks (e), ALP activity of BMSCs after 3, 7, and 14 days (f) and OCN protein expression (g).

* $p < 0.05$, ** $p < 0.01$, *** $p < 0.001$, compared with the Control group; #### $p < 0.001$, compared with the SFFHM group, (d) $n = 6$, (e) $n = 3$, (f) $n = 5$, (g) $n = 4$, ns = not significant.

corresponding two-dimensional representative images are shown in Figure 6(a). The new bone formation in the defects was detected 4, 6 and 8 weeks after implantation. We observed that control, SFF, SFFH and SFFM scaffolds appeared to have a weak effect on mineralization at week 4; however, SFFHM enhanced bony ingrowth into the defect area. At week 6, each group of bone tissue had different degrees of growth and showed a similar trend as that at 4 weeks. The Control group remained wide open with smaller amounts of new bone tissue at weeks 4 and 6, whereas the bone formation of the SFFH and SFFM scaffolds was not as good as that of the SFFHM scaffold, and there was only some new bone generation at the periphery of the defect in the Control (untreated) scaffold groups at week 6 and 8, while SFF scaffolds had worse osteogenic function than other scaffolds. By week 8, the defect with implanted SFFHM scaffold was completely filled with mineralized (mature) bone tissue, and the bone marrow cavity also returned to a smooth state.

Further, the regenerated bone volume/total volume (BV/TV) ratio (Figure 6(b)), trabecular number (Tb.N) (Figure 6(c)) and bone mineral density (BMD) (Figure 6(d)) were determined using the obtained micro-CT results. The BV/TV of new bone in the SFFHM scaffold group ($38.58 \pm 1.43\%$), SFFM group ($26.43 \pm 1.13\%$), SFFH group ($15.35 \pm 0.84\%$), SFF group ($14.12 \pm 0.50\%$) and Control group ($11.22 \pm 0.90\%$) at week 8 were consistent with the micro-CT images above. The Tb.N of bone defect area in the SFFHM scaffold group showed a relatively obvious advantage over the Control group at each time point. Consistently, the BMD of new bone in the SFFHM scaffolds ($402.0 \pm 25.24 \text{ mg/m}^3$) was similar to that in the SFFM scaffolds ($376.0 \pm 6.56 \text{ mg/m}^3$). However, the BMD of SFFHM was significantly higher than that in the SFFH scaffolds ($317.3 \pm 21.46 \text{ mg/m}^3$), SFF scaffolds ($258.3 \pm 27.50 \text{ mg/m}^3$), and Control scaffolds ($255.7 \pm 9.02 \text{ mg/m}^3$) at week 8. Otherwise, compared to the Control group, with the exception of the SFF

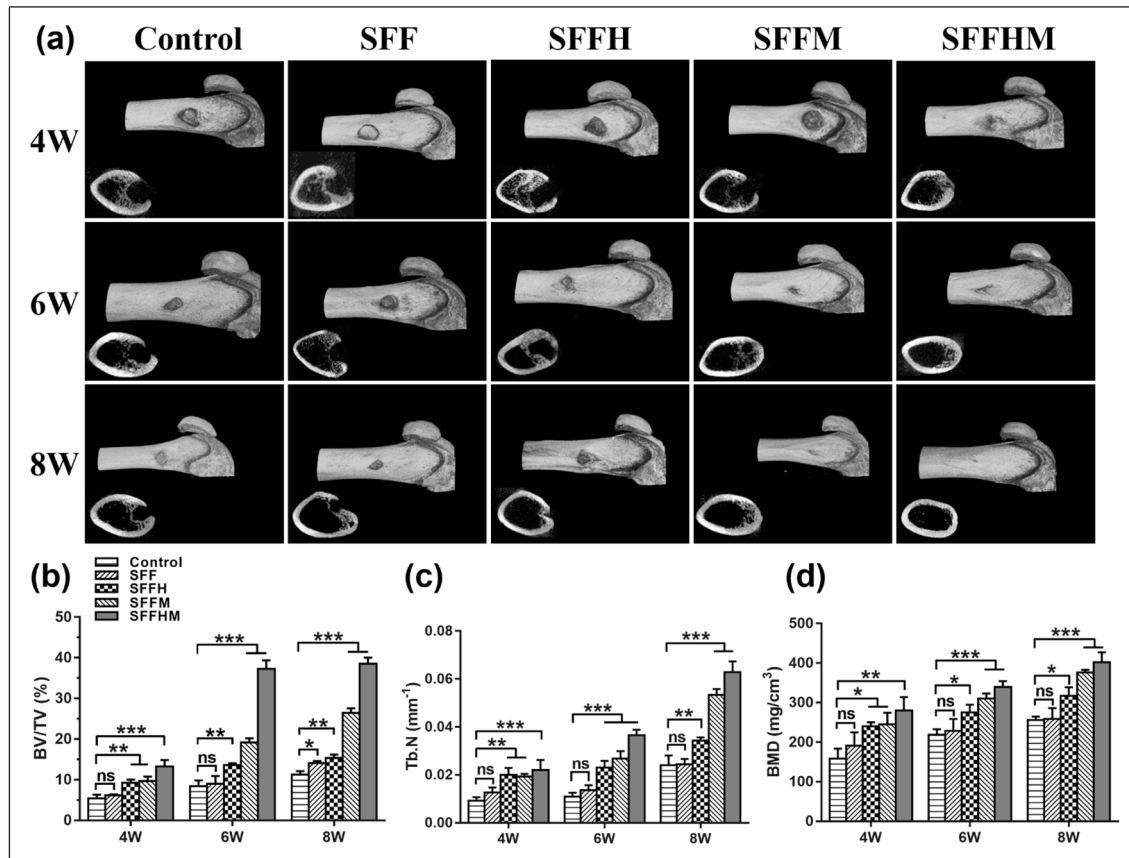


Figure 6. Imaging examination and quantitative analysis of bone tissue. (a) Representative 3D reconstructed images and tomography radiographs of new bone formation within bone tunnels at 4, 6 and 8 weeks after surgery. Micro computed tomography (Micro-CT) quantified analysis of (b) Bone volume fraction (BV/TV). (c) Trabecular number (Tb.N) and (d) Bone mineral density (BMD).

(* $p < 0.05$, ** $p < 0.01$, *** $p < 0.001$, ns = not significant, $n = 3$).

scaffolds group, the other groups all showed increased BV/TV, Tb. N, and BMD values in a time-dependent fashion with an integration between the implanted scaffold and the surrounding tissues. Overall, the data indicated the strong potential and excellent osteoconductive capacity of the SFFHM scaffolds to promote new bone growth in vivo.

Histological analysis

Next, we assessed the bone-healing properties in SD rats with femur defects as well as the significance of MgO and HAp in the composite scaffolds by histological analysis; haematoxylin and eosin (H&E) staining and Masson's trichrome staining (MTS) were performed to study the formation of new bone in the defect sites of femur. At 4 weeks, the H&E staining (Figure 7(a)) of scaffold-implanted femur defects presents that there were a large number of scaffold profiles in the four material group. Among the SFFM and SFFHM groups, many osteoblasts and cell matrix grew into the scaffold from surrounding tissues, while the Control group was mainly fibroblasts

and hyperplastic fibrous tissue. Most of the residual material was eliminated after 8 weeks, and the defect area was covered by bone collagen and new bone tissue. However, a large amount of fibroblasts were visible at the bone defect in the Control group. Furthermore, the SFFH, SFFM and SFFHM groups showed good reshaping of the bone defect and re-opening of the bone marrow cavity. There was more new bone formation and thicker bone matrix in SFFHM scaffold group than in other scaffolds, and least bone formation was observed in Control group.

Furthermore, the formation of new collagenous tissue was observed by the MTS staining assay (Figure 7(b)) which revealed osteoid as blue staining in the sections. The dense blue colored bone collagen that almost filled the defect area in the SFFHM group, especially the most obvious in the early 4th week. Whereas, the Control group was mainly fibrous tissue, and there were loose collagen and less primitive bone tissue in the Control and SFF scaffold groups. SFFHM composite scaffolds displayed a conspicuous increase in initial bone tissue ingrowth, as evidenced by less unfilled interspaces. With the extension of time to

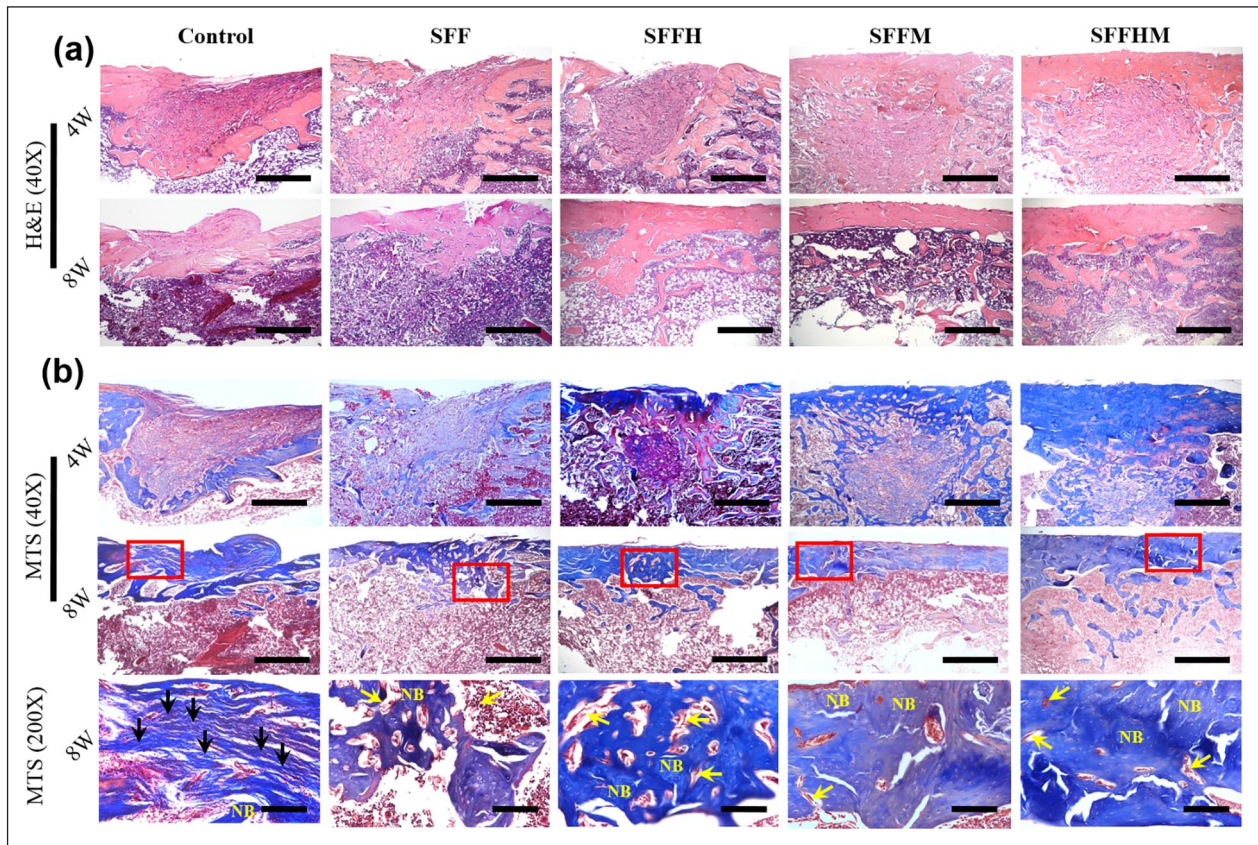


Figure 7. Histological evaluations of the regeneration of bone defects at 4 and 8 weeks after surgery, representative images of H&E staining (a) (scale bar = 100 μ m, 40 \times) and corresponding Masson's trichrome staining, (b) scale bar: upper two rows 100 μ m (40 \times), and bottom row 20 μ m (200 \times), respectively. NB represent new bone, black arrows indicate fibrous tissue, yellow arrows shows remnant of scaffolds.

8 weeks, the collagen of Control group increased relatively, however, the collagen in all scaffold groups decreased compared with that at 4 weeks, indicating that it was replaced by new bone tissue. Each group of scaffolds have a very small amount of residue at 8 weeks after surgery, and it is gradually replaced by new tissue. The result shown that SFFHM scaffolds induced more bone collagen regeneration and further forming new bone tissue than the other type scaffolds attributing to the combined action of HAp and MgO added simultaneously in the scaffold.

Bone tissue related marker proteins ALP and Col-I (4 weeks after surgery) and OCN (8 weeks after surgery) were further confirmed by immunofluorescence staining and immunohistochemistry staining. The fluorescence intensity of Col-I positive staining in the SFFHM group and SFFM group were significantly higher than other groups (Figure 8(a) and (c)). Moreover, the highest intense brownish black staining of ALP, Col-I and OCN in the SFFHM scaffold-treated defects in all groups (Figure 8(b), (d)–(f)). Collectively, the results were ascribed to the collective effect of Mg ion release, the weak alkaline micro-environment and HAp from SFFHM scaffolds, and these

findings demonstrated that the SFFHM scaffold can efficiently promote bone regeneration when transplanted into the bone defect area.

Discussion

Multi-functional bone repair composite scaffolds will provide a new development direction and clinical treatment strategy for orthopaedics and bone tissue engineering. In particular, a composite scaffold or an extracellular matrix (ECM) can be synthesized by natural materials with good biocompatibility, osteogenic induction, and progressive degradation and absorption.⁵⁰ This biomaterial scaffold can provide three-dimensional space for cells survival, which is beneficial for cells to obtain sufficient nutrients, exchange gas, exclude metabolic waste, and establishment of mechanical interlock between the host tissue and the scaffold.⁵¹ The scaffold is implanted into the bone defect site, and the BMSCs continuously adhere, proliferate and osteogenic differentiate while the material is gradually degraded, thereby achieving the purpose of repairing a bone tissue defect. The mechanical strength, degradation

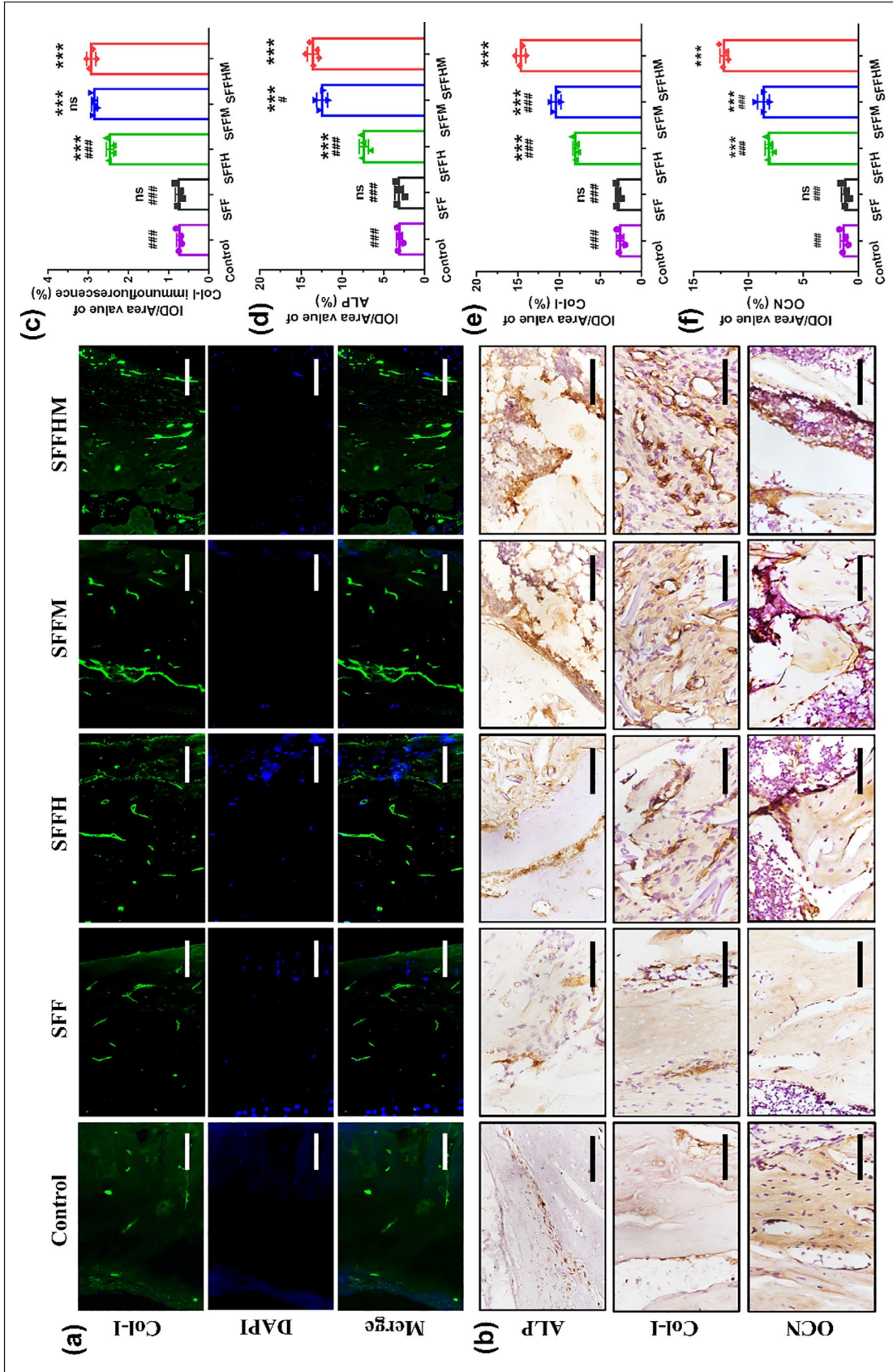


Figure 8. Immunostaining of bone tissue specimens at 4 and 8 weeks: (a and c) Immunofluorescence images of Col-I expression and quantitative analysis for tissue sections after scaffolds implantation 4 weeks (green: OCN; blue: DAPI), (b) immunohistochemical images of ALP, Col-I and OCN expression, scale bar = 100 μ m (400 \times). (d–f) Quantitative analysis of new bone formation expressed as ALP, Col-I and OCN levels. *** $p < 0.001$, compared with Control group; # $p < 0.05$, ## $p < 0.001$, ### $p < 0.0001$, compared with SFFHM group; $n = 4$, ns = not significant).

rate, local microenvironment and sustained release of certain metal ions of scaffolds are also critical factors for bone repair. However, materials that combine these characteristics together have not been reported.

In this study, mimicking ECM of bone,⁵² we designed and manufactured an biomimetic multifunctional composite scaffold material incorporating HAp and MgO that uses silk fiber and silk fibroin extracted from natural silk-worm cocoons. The silk fibrous network significantly enhances the compressive modulus of the SFFHM composite scaffold. The gel formed by silk fibroin was filled inside and on the surface of the composite scaffold to form a physical barrier that ensured the sustained and smooth release of HAp and Mg ions during the scaffold degradation, and a weak alkaline microenvironment for cell survival formed around the scaffold. It happens that this scaffold had a suitable degradation rate (34.8 ± 2.51 %) at 6 weeks (Figure 2(d)) *in vitro* and it was almost completely degraded at 8 weeks *in vivo* (Figure 7(b)), which allowed the migration of osteogenic cells to the center of the bone defect.⁵³ In other words, the degradation and resorption of scaffolds with time matching the remodeling kinetics of host bone tissue.⁵⁴ HAp, a dominant inorganic of bone, can provide a nucleation center for mineralization to aid bone formation and reconstruction. Since calcium ions bound to hydrophilic groups, silk fibroin governed the nucleation and particle size of HAp, which may affect topological characteristics and surface roughness, thereby regulating cell-matrix interactions, which is an important component of bone regeneration. However, the silk fibrous network and HAp significantly enhances the compressive modulus of the composite SFFHM scaffold (7.11 ± 1.69 MPa) (Figure 3(b)), and the mechanical strength of the scaffold implanted in the bone defect is also an important factor for bone healing, especially for large areas, load-bearing bone or long segmental bone defects. It is reported that the compressive strength of adult dense bone and cancellous bone is 100–230 MPa and 2–12 MPa, respectively.⁵⁵ Although the mechanical strength of our scaffold is much lower than that of dense bone, it is much higher than the mechanical strength of most reported scaffolds,^{56–58} and this scaffold is more suitable for bone defects near the joint position.

The results above showed that MgO at an appropriate concentration (low content of 1 wt.%) can exert stimulatory effects on the osteogenic proliferation and differentiation of BMSCs. Interestingly, the weak alkaline microenvironment formed around the composite scaffold also played an important role in the proliferation and differentiation of SD rat BMSCs. Several citations in the literature have shown that a weak alkaline environment around the scaffolds can promote the osteogenic activities of osteoblasts and BMSCs.^{59,60} However, for BMSCs cultured in a highly alkaline microenvironment, the growth and proliferation are inhibited, which may result from alkalosis.⁶¹ Our research results in Figures 2(c) and 3(d)

are consistent with the conclusions reported previously. Mg ions and weak alkaline microenvironment produced by MgO can induce the mineralization of minerals (calcium, phosphorus and phosphate) during the process of osteogenesis, and they also effectively promote the osteogenic differentiation of BMSCs and bone healing. Here, Mg may promote bone formation through the reported mechanism, which is ascribed to the upregulation of neuronal calcitonin gene-related polypeptide- α (CGRP) expression via Mg ions stimulating the sensory nerve, and increases in CGRP can improve the osteogenic differentiation ability of periosteum-derived stem cells and induce microvascular dilation.^{62,63} Otherwise, some studies have reported that Mg ions can stimulate the proliferation of BMSCs and promote BMSCs differentiation into osteoblasts through regulation of transient receptor potential melastatin 7 (TRPM7) channel activity and acceleration of notch intracellular domain translocation.^{64–66} It is worth mentioning that we did not detect the serum magnesium ion concentration, which can cause cardiovascular, renal, liver disease, as well as metabolism disorder if present in higher concentrations.⁶⁷ However, not only all the experimental animals were healthy before being sacrificed, but also there was no obvious inflammatory cell infiltration in H&E staining of bone tissue, which proved that all the composite scaffold has good biocompatibility.

Osteogenic activity, an important property of biomaterial, is a necessary procedure for the differentiation of BMSCs into osteoblasts followed by ECM mineral deposition and forming bone tissue. The ARS staining confirmed the deposition of calcium phosphate in the BMSCs culture and differentiation system. Figure 5(a) and (d) showed that ARS chelated with Ca^{2+} through mineralized ECM to make the most bright-red stains in SFFHM group comparing to other groups. The results demonstrated that the collective effect of MgO and HAp components in SFFHM composite scaffold promoted the mineral deposition of differentiated BMSC and the mineralization of ECM. Furthermore, SFFHM scaffold also displayed higher ALP activity. ALP, a major enzyme in the process of bone mineralization, is an early stage marker of osteoblastic differentiation.^{68,69} The ability of osteogenic differentiation of BMSCs cultured in scaffolds leaching medium was also investigated by immunofluorescence of OCN protein expression. This result confirms that the SFFHM scaffold can significantly promote the expression of OCN protein at day 21, a specific marker of BMSCs osteogenic differentiation (Figure 5(c) and (g)). The incorporation of MgO provides Mg^{2+} and a weak alkaline microenvironment for maintenance of osteogenic traits of osteoblasts, which is discovered in MgO loaded scaffold when compared to other groups without MgO. Similar observations were noticed by Tan et al.⁷⁰ who showed that the alkaline microenvironment and releasing Mg^{2+} may produce a synergistic effect on ALP, when cultured with rBMSCs for osteogenic differentiation. To further investigate the

osteogenic potential of composite scaffolds at a molecular level in vivo, we examined the gene expression levels of ALP, Col-I and OCN of SD rats bone tissue section,⁷¹ respectively. Col-I is the main component of the ECM involved in the repair of tissue such as bone, skin, tendon, ligament and dentine,⁷² and Mg ions can enhance Col-I expression.⁷³ OCN, one of the most important marker proteins in osteoblast differentiation and mineralization, is secreted solely by osteoblasts and regulates bone building,⁷⁴ which is also representative indexes for further bone maturation.⁷⁵ Studies have shown that fibers-incorporated scaffold enhanced ALP activity of BMSCs by the reason of increase in mechanical strength.⁷⁶ Coincidentally, the composite scaffold SFFHM exhibits higher ALP protein expression in bone tissue (Figure 8(b) and (d)), which may also be affected by the increased mechanical strength caused by F and HAp. The maximum Col-I protein expression was observed by immunohistochemistry and immunofluorescence of specimens in SFFHM scaffold group compared with Control group and other scaffold groups. This data is in agreement with Masson's trichrome staining where these scaffolds loaded MgO (SFFM/SFFHM) supported cell proliferation and differentiation suggesting mineralization and maturation of ECM. The higher OCN protein expression of the SFFHM scaffold at 8 weeks (Figure 8(b) and (f)) is consistent with the trend of OCN produced by differentiation of BMSCs in vitro at 3 weeks. At the same time, HAp in scaffolds exhibit bone conduction and bone regeneration capabilities in vivo (Figures 6 and 7).

In the further study, the related mechanism for SFFHM composite scaffold to stimulate the expression of bone-related markers should be investigated. However, It is safe to say that the composite scaffolds formed by adding HAp or MgO (SFFH/SFFM) or both of them (SFFHM) using SF/F as a framework can stimulate the proliferation and differentiation of BMSCs to different degrees, and promote the formation of new bone tissue, especially the effect of the SFFHM composite scaffold is the most powerful. From all of the above descriptions, the results presented here suggest that a novel composite scaffold with incorporation MgO and HAp in silk fibroin-fibers has superior physical and chemical properties for cell supportiveness. It can stimulate a series in the evolution of BMSCs, such as cell attachment, proliferation, collagen deposition and osteogenic differentiation, and accelerate the formation and reconstruction of new bone tissue.

Conclusion

In this study, a novel composite scaffold based on natural biomacromolecules silk fibroin and silk fibers was explored with an uncomplicated manufacturing process and accessible components to promote bone repair. By chemical precipitation and freeze drying, we evenly incorporated

different concentrations of MgO and deposited the mineralized HAp. When SFFHM scaffold with mass proportion of 1 wt.% MgO was used as active ingredient, the scaffold released a certain concentration of Mg²⁺ and created a suitable weak alkaline microenvironment with pH 7.2-8.01, which exhibited obvious effect of promoting BMSCs proliferation. Moreover, this scaffold has superior physical and chemical properties, cell activity and osteogenic activity. The comprehensive evaluation of cellular and animal experiments on ALP activity, deposition of calcium salt, deposition of collagenous deposition and expression of bone-related marker proteins (ALP, Col-I and OCN) further attested the superior osteogenic potential of this composite scaffolds. After being implanted into the SD rat femur defect, the composite scaffold with good biocompatibility can significantly facilitate in situ bone regeneration and bone reconstruction. In view of the above advantages, SFFHM composite scaffold provide improved bone regeneration ability and it will expand the scope of research and development of biomedical materials, suggesting a promising tissue engineered graft for clinical application to treat bone defects.

Declaration of conflicting interests

The author(s) declared no potential conflicts of interest with respect to the research, authorship, and/or publication of this article.

Funding

The author(s) disclosed receipt of the following financial support for the research, authorship, and/or publication of this article: This research was supported by the National Natural Science Foundation of China (Grant No. 82060347), the National Natural Science Foundation of China (Grant No. 81772316), the National Natural Science Foundation of China (Grant No. 81460339), Hainan Provincial Foundation for Education Department (Grant No. Hnky2019ZD-28) and Medical Health Science and Technology Project of Zhejiang Provincial Health Commission (2020KY365).

ORCID iD

Ziquan Wu  <https://orcid.org/0000-0003-0100-1155>

References

1. Fernandez de Grado G, Keller L, Idoux-Gillet Y, et al. Bone substitutes: a review of their characteristics, clinical use, and perspectives for large bone defects management. *J Tissue Eng* 2018, 9: 2041731418776819.
2. Sudakaran SV, Venugopal JR, Vijayakumar GP, et al. Sequel of MgO nanoparticles in PLACL nanofibers for anti-cancer therapy in synergy with curcumin/beta-cyclodextrin. *Mater Sci Eng C Mater Biol Appl* 2017, 71: 620–628.
3. Çakır B, Budama Akpolat L, Topel Ö, et al. Synthesis of ZnO nanoparticles using PS-b-PAA reverse micelle cores for UV protective, self-cleaning and antibacterial textile applications. *Colloid Surface A* 2012, 414: 132-139.

- Prucek R, Tucek J, Kilianova M, et al. The targeted antibacterial and antifungal properties of magnetic nanocomposite of iron oxide and silver nanoparticles. *Biomaterials* 2011; 32: 4704–4713.
- Trujillo N, Oldinski R, Ma H, et al. Antibacterial effects of silver-doped hydroxyapatite thin films sputter deposited on titanium. *Mater Sci Eng* 2012; 32: 2135–2144.
- Syed-Picard FN, Shah GA, Costello BJ, et al. Regeneration of periosteum by human bone marrow stromal cell sheets. *J Oral Maxillofac Surg* 2014; 72: 1078–1083.
- Wang P, Zhao L, Liu J, et al. Bone tissue engineering via nanostructured calcium phosphate biomaterials and stem cells. *Bone Res* 2014; 2: 139–151.
- Wu C, Chen Z, Yi D, et al. Multidirectional effects of Sr-, Mg-, and Si-containing bioceramic coatings with high bonding strength on inflammation, osteoclastogenesis, and osteogenesis. *ACS Appl Mater Interfaces* 2014; 6: 4264–4276.
- O'Donnell MD and Hill RG. Influence of strontium and the importance of glass chemistry and structure when designing bioactive glasses for bone regeneration. *Acta Biomater* 2010; 6: 2382–2385.
- Zhao D, Witte F, Lu F, et al. Current status on clinical applications of magnesium-based orthopaedic implants: a review from clinical translational perspective. *Biomaterials* 2017; 112: 287–302.
- Bose S, Roy M and Bandyopadhyay A. Recent advances in bone tissue engineering scaffolds. *Trends Biotechnol* 2012; 30: 546–554.
- Tian L, Sheng Y, Huang L, et al. An innovative Mg/Ti hybrid fixation system developed for fracture fixation and healing enhancement at load-bearing skeletal site. *Biomaterials* 2018; 180: 173–183.
- Xavier JR, Thakur T, Desai P, et al. Bioactive nanoengineered hydrogels for bone tissue engineering: a growth-factor-free approach. *ACS Nano* 2015; 9: 3109–3118.
- Kim H, Che L, Ha Y, et al. Mechanically-reinforced electrospun composite silk fibroin nanofibers containing hydroxyapatite nanoparticles. *Mater Sci Eng C Mater Biol Appl* 2014; 40: 324–335.
- Panda N, Bissoyi A, Pramanik K, et al. Development of novel electrospun nanofibrous scaffold from P. Ricini And A. Mylitta silk fibroin blend with improved surface and biological properties. *Mater Sci Eng C Mater Biol Appl* 2015; 48: 521–532.
- Bhumiratana S, Grayson WL, Castaneda A, et al. Nucleation and growth of mineralized bone matrix on silk-hydroxyapatite composite scaffolds. *Biomaterials* 2011, 32: 2812–2820.
- Mandal BB and Kundu SC. Osteogenic and adipogenic differentiation of rat bone marrow cells on non-mulberry and mulberry silk gland fibroin 3D scaffolds. *Biomaterials* 2009; 30: 5019–5030.
- Zhang Q, Zhao Y, Yan S, et al. Preparation of uniaxial multichannel silk fibroin scaffolds for guiding primary neurons. *Acta Biomater* 2012; 8: 2628–2638.
- Yan LP, Oliveira JM, Oliveira AL, et al. Macro/microporous silk fibroin scaffolds with potential for articular cartilage and meniscus tissue engineering applications. *Acta Biomater* 2012; 8: 289–301.
- Ogose A, Hotta T, Kawashima H, et al. Comparison of hydroxyapatite and beta tricalcium phosphate as bone substitutes after excision of bone tumors. *J Biomed Mater Res B Appl Biomater* 2005; 72: 94–101.
- Frohbergh ME, Katsman A, Botta GP, et al. Electrospun hydroxyapatite-containing chitosan nanofibers crosslinked with genipin for bone tissue engineering. *Biomaterials* 2012; 33: 9167–9178.
- Kim SS, Sun Park M, Jeon O, et al. Poly(lactide-co-glycolide)/hydroxyapatite composite scaffolds for bone tissue engineering. *Biomaterials* 2006; 27: 1399–1409.
- Ho MH, Yao CJ, Liao MH, et al. Chitosan nanofiber scaffold improves bone healing via stimulating trabecular bone production due to upregulation of the Runx2/osteocalcin/alkaline phosphatase signaling pathway. *Int J Nanomedicine* 2015; 10: 5941–5954.
- Ou L, Lan Y, Feng Z, et al. Functionalization of SF/HAP Scaffold with GO-PEI-miRNA inhibitor complexes to enhance bone regeneration through activating transcription factor 4. *Theranostics* 2019; 9: 4525–4541.
- Ko E, Lee JS, Kim H, et al. Electrospun silk fibroin nanofibrous scaffolds with two-stage hydroxyapatite functionalization for enhancing the osteogenic differentiation of human adipose-derived mesenchymal stem cells. *ACS Appl Mater Interfaces* 2018; 10: 7614–7625.
- Jang HL, Jin K, Lee J, et al. Revisiting whitlockite, the second most abundant biomineral in bone: nanocrystal synthesis in physiologically relevant conditions and biocompatibility evaluation. *ACS Nano* 2014; 8: 634–641.
- Abdallah MN, Eimar H, Bassett DC, et al. Diagenesis-inspired reaction of magnesium ions with surface enamel mineral modifies properties of human teeth. *Acta Biomater* 2016; 37: 174–183.
- Castiglioni S, Cazzaniga A, Albisetti W, et al. Magnesium and osteoporosis: current state of knowledge and future research directions. *Nutrients* 2013; 5: 3022–3033.
- Yoshizawa S, Brown A, Barchowsky A, et al. Magnesium ion stimulation of bone marrow stromal cells enhances osteogenic activity, simulating the effect of magnesium alloy degradation. *Acta Biomater* 2014; 10: 2834–2842.
- Leidi M, Delleria F, Mariotti M, et al. High magnesium inhibits human osteoblast differentiation in vitro. *Magn Res* 2011; 24: 1–6.
- Wang Y, Wei M, Gao J, et al. Corrosion process of pure magnesium in simulated body fluid. *Mater Lett* 2008; 62: 2181–2184.
- Ke D, Tarafder S, Vahabzadeh S, et al. Effects of MgO, ZnO, SrO, and SiO in tricalcium phosphate scaffolds on in vitro gene expression and in vivo osteogenesis. *Mat Sci Eng C- Mater* 2019; 96: 10–19.
- Hickey DJ, Ercan B, Sun L, et al. Adding MgO nanoparticles to hydroxyapatite-PLLA nanocomposites for improved bone tissue engineering applications. *Acta Biomater* 2015; 14: 175–184.
- Brandao-Burch A, Utting JC, Orriss IR, et al. Acidosis inhibits bone formation by osteoblasts in vitro by preventing mineralization. *Calcif Tissue Int* 2005; 77: 167–174.
- Kato Y, Ozawa S, Miyamoto C, et al. Acidic extracellular microenvironment and cancer. *Cancer Cell Int* 2013; 13: 89.
- Shen Y, Liu WC, Wen C, et al. Bone regeneration: importance of local pH - Strontium-doped borosilicate scaffold. *J Mater Chem* 2012; 22: 8662–8670.

37. Liu W, Wang T, Yang C, et al. Alkaline biodegradable implants for osteoporotic bone defects—importance of microenvironment pH. *Osteoporos Int* 2016; 27: 93–104.
38. Meghji S, Morrison MS, Henderson B, et al. pH dependence of bone resorption: mouse calvarial osteoclasts are activated by acidosis. *Am J Physiol Endocrinol Metab* 2001; 280: E112–E119.
39. Arnett TR. Extracellular pH regulates bone cell function. *J Nutr* 2008; 138: 415s–418s.
40. Hughes EA, Parkes A, Williams RL, et al. Formulation of a covalently bonded hydroxyapatite and poly(ether ether ketone) composite. *J Tissue Eng* 2018; 9: 2041731418815570.
41. Lee DH, Tripathy N, Shin JH, et al. Enhanced osteogenesis of beta-tricalcium phosphate reinforced silk fibroin scaffold for bone tissue biofabrication. *Int J Biol Macromol* 2017; 95: 14–23.
42. Nazarov R, Jin HJ and Kaplan DL. Porous 3-D scaffolds from regenerated silk fibroin. *Biomacromolecules* 2004; 5: 718–726.
43. Mandal BB and Kundu SC. Non-bioengineered silk fibroin protein 3D scaffolds for potential biotechnological and tissue engineering applications. *Macromol Biosci* 2008; 8: 807–818.
44. Song JE, Tripathy N, Cha SR, et al. Three-dimensional duck's feet collagen/PLGA scaffold for chondrification: role of pore size and porosity. *J Biomater Sci Polym Ed* 2018; 29: 932–941.
45. Karageorgiou V and Kaplan D. Porosity of 3D biomaterial scaffolds and osteogenesis. *Biomaterials* 2005; 26: 5474–5491.
46. Cao Y and Wang B. Biodegradation of silk biomaterials. *Int J Mol Sci* 2009; 10: 1514–1524.
47. Kang H, Wong DSH, Yan X, et al. Remote control of multimodal nanoscale ligand oscillations regulates stem cell adhesion and differentiation. *ACS Nano* 2017; 11: 9636–9649.
48. Pati F, Song TH, Rijal G, et al. Ornamenting 3D printed scaffolds with cell-laid extracellular matrix for bone tissue regeneration. *Biomaterials* 2015; 37: 230–241.
49. Xue W, Krishna BV, Bandyopadhyay A, et al. Processing and biocompatibility evaluation of laser processed porous titanium. *Acta Biomater* 2007; 3: 1007–1018.
50. Hofmann S, Hagenmuller H, Koch AM, et al. Control of in vitro tissue-engineered bone-like structures using human mesenchymal stem cells and porous silk scaffolds. *Biomaterials* 2007; 28: 1152–1162.
51. Takahashi Y and Tabata Y. Effect of the fiber diameter and porosity of non-woven PET fabrics on the osteogenic differentiation of mesenchymal stem cells. *J Biomater Sci Polym Ed* 2004; 15: 41–57.
52. Langer R and Vacanti JP. Tissue engineering. *Science* 1993; 260: 920–926.
53. Huebsch N, Lippens E, Lee K, et al. Matrix elasticity of void-forming hydrogels controls transplanted-stem-cell-mediated bone formation. *Nat Mater* 2015; 14: 1269–1277.
54. Porter J, Ruckh T and Popat K. Bone tissue engineering: a review in bone biomimetics and drug delivery strategies. *Biotechnol Progr* 2009; 25: 1539–1560.
55. Cheng G, Yin C, Tu H, et al. Controlled co-delivery of growth factors through layer-by-layer assembly of core-shell nanofibers for improving bone regeneration. *ACS Nano* 2019; 13: 6372–6382.
56. Gupta P, Adhikary M, Joseph Christakiren M, et al. Biomimetic, osteoconductive non-mulberry silk fiber reinforced tricomposite scaffolds for bone tissue engineering. *ACS Appl Mater Interfaces* 2016; 8: 30797–30810.
57. Song JE, Tripathy N, Lee DH, et al. Quercetin inlaid silk fibroin/hydroxyapatite scaffold promotes enhanced osteogenesis. *ACS Appl Mater Interfaces* 2018; 10: 32955–32964.
58. Zhang XY, Chen YP, Han J, et al. Biocompatible silk fibroin/carboxymethyl chitosan/strontium substituted hydroxyapatite/cellulose nanocrystal composite scaffolds for bone tissue engineering. *Int J Biol Macromol* 2019; 136: 1247–1257.
59. Shen Y, Liu W, Lin K, et al. Interfacial pH: a critical factor for osteoporotic bone regeneration. *Langmuir* 2011; 27: 2701–2708.
60. Li Q, Wang D, Qiu J, et al. Regulating the local pH level of titanium via Mg-Fe layered double hydroxides films for enhanced osteogenesis. *Biomater Sci* 2018; 6: 1227–1237.
61. Dong C, Song D, Cairney J, et al. Antibacterial study of Mg(OH)₂ nanoplatelets. *Mater Res Bull* 2011; 46: 576–582.
62. Zhang Y, Xu J, Ruan YC, et al. Implant-derived magnesium induces local neuronal production of CGRP to improve bone-fracture healing in rats. *Nat Med* 2016; 22: 1160–1169.
63. Tang P, Duan C, Wang Z, et al. NPY and CGRP inhibitor influence on ERK pathway and macrophage aggregation during fracture healing. *Cell Physiol Biochem* 2017; 41: 1457–1467.
64. Diaz-Tocados JM, Herencia C, Martinez-Moreno JM, et al. Magnesium chloride promotes osteogenesis through notch signaling activation and expansion of mesenchymal stem cells. *Sci Rep* 2017; 7: 7839.
65. Castiglioni S, Romeo V, Locatelli L, et al. The simultaneous downregulation of TRPM7 and MagT1 in human mesenchymal stem cells in vitro: effects on growth and osteogenic differentiation. *Biochem Biophys Res Commun* 2019; 513: 159–165.
66. Castiglioni S, Romeo V, Locatelli L, et al. TRPM7 and MagT1 in the osteogenic differentiation of human mesenchymal stem cells in vitro. *Sci Rep* 2018; 8: 16195.
67. Akhtar ML, Ullah H and Hamid M. Magnesium, a drug of diverse use. *J Pak Med Assoc* 2011; 61: 1220–1225.
68. Mikami Y, Tsuda H, Akiyama Y, et al. Alkaline phosphatase determines polyphosphate-induced mineralization in a cell-type independent manner. *J Bone Miner Metab* 2016; 34: 627–637.
69. Ohara N, Hayashi Y, Yamada S, et al. Early gene expression analyzed by cDNA microarray and RT-PCR in osteoblasts cultured with water-soluble and low molecular chito oligosaccharide. *Biomaterials* 2004; 25: 1749–1754.
70. Tan J, Wang D, Cao H, et al. Effect of local alkaline microenvironment on the behaviors of bacteria and osteogenic cells. *ACS Appl Mater Interfaces* 2018; 10: 42018–42029.
71. Al Subaie A, Emami E, Tamimi I, et al. Systemic administration of omeprazole interferes with bone healing and

- implant osseointegration: an in vivo study on rat tibiae. *J Clin Periodontol* 2016; 43: 193–203.
72. Branco da Cunha C, Klumpers DD, Li WA, et al. Influence of the stiffness of three-dimensional alginate/collagen-I interpenetrating networks on fibroblast biology. *Biomaterials* 2014; 35: 8927–8936.
 73. Jung YR, Lee EK, Kim DH, et al. Upregulation of collagen expression via PPARbeta/delta activation in aged skin by magnesium lithospermate B from salvia miltiorrhiza. *J Nat Prod* 2015; 78: 2110–2115.
 74. Feng B, Weng J, Yang BC, et al. Characterization of titanium surfaces with calcium and phosphate and osteoblast adhesion. *Biomaterials* 2004; 25: 3421–3428.
 75. Ratanavaraporn J, Furuya H, Kohara H, et al. Synergistic effects of the dual release of stromal cell-derived factor-1 and bone morphogenetic protein-2 from hydrogels on bone regeneration. *Biomaterials* 2011; 32: 2797–2811.
 76. Mandal BB, Grinberg A, Gil ES, et al. High-strength silk protein scaffolds for bone repair. *Proc Natl Acad Sci USA* 2012; 109: 7699–7704.